





CRISPR targeting of *FOXL2* c.402C>G mutation reduces malignant phenotype in granulosa tumor cells and identifies anti-tumoral compounds

Sandra Amarilla-Quintana^{1,2}, Paloma Navarro³, Iván Hernández¹, Alejandra Ramos¹, Ana Montero-Calle⁴, Pablo Cabezas-Sainz⁵, Maria J Barrero¹, Diego Megías⁶, Borja Vilaplana-Martí¹ , Carolina Epifano¹, Déborah Gómez-Dominguez¹, Sara Monzón⁷, Isabel Cuesta⁷, Laura Sánchez⁵, Rodrigo Barderas⁴ , Jesús García-Donas³, Alberto Martín¹  and Ignacio Pérez de Castro¹ 

1 Instituto de Investigación de Enfermedades Raras, Instituto de Salud Carlos III, Madrid, Spain

2 Programa de Doctorado en Ciencias Biomédicas y Salud Pública IMIENS-UNED-ISCIII, Escuela Internacional de Doctorado de la Universidad Nacional de Educación a Distancia (EIDUNED), Madrid, Spain

3 HM Hospitales-Centro Integral Oncológico HM Clara Campal, Madrid, Spain

4 Chronic Disease Program (UFIEC), Instituto de Salud Carlos III, Madrid, Spain

5 Department of Zoology, Genetics and Physical Anthropology, Universidade de Santiago de Compostela, Lugo, Spain

6 Confocal Microscopy Unit, Instituto de Salud Carlos III, Madrid, Spain

7 Bioinformatic Unit, Instituto de Salud Carlos III, Madrid, Spain

Keywords

CRISPR; *FOXL2*; granulosa cell tumor; rare cancer

Correspondence

A. Martín and I. Pérez de Castro, Instituto de Investigación de Enfermedades Raras, Instituto de Salud Carlos III, Ctra. Majadahonda-Pozuelo km2.2, Madrid, Spain
 E-mail: almartin@usal.es, iperez@isciii.es

Forkhead box L2 (*FOXL2*) encodes a transcription factor essential for sex determination, and ovary development and maintenance. Mutations in this gene are implicated in syndromes involving premature ovarian failure and granulosa cell tumors (GCTs). This rare cancer accounts for less than 5% of diagnosed ovarian cancers and is causally associated with the *FOXL2* c.402C>G, p.C134W mutation in 97% of the adult cases (AGCTs). In this study, we employed CRISPR technology to specifically eliminate the *FOXL2* c.402C>G mutation in granulosa tumor cells. Our results show that this Cas9-mediated strategy selectively targets the mutation without affecting the wild-type allele. Granulosa cells lacking *FOXL2* c.402C>G

Abbreviations

AGCTs, adult granulosa cell tumors; AKT, AKT serine/threonine kinase; AMH, anti Müllerian hormone; BCA, bichoninic acid assay; BMF, Bcl2 modifying Factor; BPES, blepharophimosis-ptosis-epicanthus; BSA, bovine serum albumin; CALB1, calbindin 1; CAV1, caveolin 1; CAV2, caveolin 2; CD55, CD55 molecule (Cromer blood group); CDH12, cadherin 12; CDK, cyclin-dependent kinases; CHT, caudal hematopoietic tissue; COL4A5, collagen type IV alpha 5 chain; CRISPR, clustered regularly interspaced short palindromic repeats; CS, cMap connectivity scores; CSPG4, chondroitin sulfate proteoglycan 4; CYP11A1, cytochrome P450, family 11, subfamily a, polypeptide 1; CYP17, cytochrome P450 17alpha-hydroxylase/17,20-lyase; CYP19A1, cytochrome P450 Family 19 Subfamily A Member 1; DEGs, differentially expressed genes; DEPs, differentially expressed proteins; DMEM, Dulbecco modified Eagle medium; ECM, extracellular matrix; ERK1/2, mitogen-activated protein kinase 3/1; FBS, fetal bovine serum; *FOXL2*, forkhead box L2; FSH, follicular stimulant hormone; GCTs, granulosa cell tumors; GFP, green fluorescent protein; GO, gene ontology; GOBP, gene ontology biological process; GSEA, gene set enrichment analysis; GSK2β, glycogen synthase kinase 3 beta; H2B-GFP, histone 2B-green fluorescent protein; HDAC, histone deacetylase; HEK-293, immortalized human embryonic kidney cells; HLA-DRB3, major histocompatibility complex, class II, DR beta 3; HLA-DRB5, major histocompatibility complex, class II, DR beta 5; JCAD, junctional cadherin 5 associated; JGCTs, juvenile granulosa cell tumors; JPH2, junctophilin-2; KO, knock-out; KSR1, kinase suppressor of Ras 1; LMOD1, leiomodulin 1; LOX, lysyl oxidase; MAP K1, mitogen-activated protein kinase; NP-40, nonyl phenoxypolyethoxyethanol; P27, cyclin-dependent kinase inhibitor 1B; PAM, protospacer adjacent motif; PBS, phosphate-buffered saline; PCA, principal component analysis; PCR, polymerase chain reaction; PDL1, CD274 molecule; PI3K, phosphatidylinositol-4,5-bisphosphate 3-kinase catalytic subunit alpha; POF, premature ovarian failure; PVP, polyvinylpyrrolidone; RT-qPCR, real-time quantitative PCR; SDS-PAGE, sodium dodecyl-sulfate polyacrylamide gel electrophoresis; SDTW, salt dechlorinate tap water; SF-1, steroidogenic factor-1; sgRNA, single-guide RNA; SLC14A1, solute carrier family 14 member 1; spCas9, streptococcus pyogenes Cas9; StAR, steroidogenic acute regulatory protein; STR, short tandem repeat; TBS, tris-buffered saline; TGFβ, transforming growth factor beta; TMT, tandem mass tag; TSKU, tsukushi, small leucine rich proteoglycan; UHPLC, ultra-high pressure liquid chromatograph.

Present address

Centro de Investigación del Cáncer,
Universidad de Salamanca, Salamanca,
Spain

Jesús García-Donas, Alberto Martín and
Ignacio Pérez de Castro contributed equally
to this work.

(Received 10 July 2024, revised 20
November 2024, accepted 24 December
2024, available online 8 January 2025)

doi:10.1002/1878-0261.13799

exhibit a reduced malignant phenotype, with significant changes in cell proliferation and invasion. Furthermore, these modified cells are more susceptible to dasatinib and ketoconazole. Transcriptomic and proteomic analyses reveal that CRISPR-modified granulosa tumor cells shift their expression profiles towards a wild-type-like phenotype. Additionally, this altered expression signature has led to the identification of new compounds with antiproliferative and pro-apoptotic effects on granulosa tumor cells. Our findings demonstrate the potential of CRISPR technology for the specific targeting and elimination of a mutation causing GTCs, highlighting its therapeutic promise for treating this rare ovarian cancer.

1. Introduction

Granulosa cell tumors (GCTs) are a rare type of cancer, constituting less than 5% of all the ovarian neoplasms and representing the most common sex-cord stromal-derived tumors [1,2]. GCTs are classified into juvenile (JGCTs) or adult (AGCTs) types based on clinical and histopathological characteristics. JGCTs, diagnosed primarily in patients under 30 years, are very infrequent, accounting for 5% of GCTs cases. AGCTs are more common, predominantly affecting perimenopausal women. AGCTs originate from granulosa cells, which are crucial for follicle maturation and the synthesis of inhibin, estradiol, and anti-Müllerian hormone (AMH). While these hormones are normally secreted in premenopausal women, elevated serum levels of inhibin B and AMH in AGCTs patients serve as significant tumor markers [3]. Other histopathological markers used to determine tumor type and stage include androgen receptor, calretinin, SF-1, and FOXL2 [4,5].

Despite most AGCT cases are diagnosed at stage I due to the slow growth of these tumors, advanced stages decrease the 10-year survival rate and increase relapse risk [2]. Initial treatment typically involves surgery, including total hysterectomy and bilateral salpingo-oophorectomy in older women, with more conservative surgery options for those younger women with early-stage GCT. Adjuvant chemotherapy with platinum-based combinations is frequently administered for locally advanced disease, though its benefits remain unclear. Recurrences can occur decades after initial surgery, typically involving the peritoneal cavity, though visceral metastasis have also been reported [6–8]. Platinum-based chemotherapy may induce partial responses in recurrent disease but is not curative [9]. Various drugs, including tyrosine-kinase inhibitors

and hormone therapies like aromatase inhibitors, have been evaluated in clinical trials and series of cases [10–12]. Unfortunately, disease stabilization rather than significant tumor reduction is often observed, likely due to the slow growth of AGCTs rather than drug efficacy.

The most prominent molecular characteristic of AGCTs is a single-nucleotide mutation in the *FOXL2* gene, present in 95–97% of the cases and first described in 2009 [13]. This somatic mutation, occurring in heterozygosity, is a missense point mutation (C402G; Cys134Trp) specific to AGCTs and rarely seen in JGCTs [14]. FOXL2, a forkhead transcription factor, is mainly expressed in granulosa cells and eyelids in mammals and is associated with BPES syndrome type I (blepharophimosis-ptosis-epicanthus) [15–17] and POF (premature ovarian failure) [18]. Depletion of FOXL2 leads to a lack of primordial follicles, due to granulosa cell differentiation problems that induce atresia, affecting directly to the female fertility [19]. In animal models and during embryonic stages, FOXL2 has been described as a marker of ovarian differentiation [20,21]. In fact, FOXL2 is implicated in ovary development and maintenance through the regulation of PI3K, ERK, and Smad pathways, among others [22–24]. Furthermore, FOXL2 is involved in relevant biological processes related to cholesterol metabolism, apoptosis, cell proliferation, and differentiation, as well as immunomodulation [25]. The *FOXL2* c.402C>G, p.C134W mutation alters the FOXL2 DNA-binding domain, leading to alterations in its transcriptional regulatory capacity. Thus, FOXL2 C134W is described to form dimers with Smad proteins, a crucial step for inducing the transcriptional activation of genes involved in

survival, proliferation and epithelial to mesenchymal transition, which culminates in the development of AGCTs [26].

Given the presence of this single-nucleotide mutation, CRISPR-Cas9 technology is an ideal tool to investigate the impact of deleting *FOXL2* c.402C>G on tumor phenotype and to explore the underlying molecular mechanisms. Understanding these aspects can lead to new therapeutic strategies, potentially improving survival and health outcomes of AGCT patients.

In this study, we demonstrate that eliminating *FOXL2* c.402C>G induces anti-tumor properties, increases sensitivity to certain therapeutic agents and identifies dysregulated pathways and processes that could be targeted by repurposed drugs.

2. Materials and methods

Details of reagents, kits, plasmid, antibodies, and other resources included in this work are listed in Table 1.

2.1. Cell lines

We have used the KGN cell line (Riken BioResource: RCB1154; RRID: CVCL_0375) established from a 63-year-old Japanese ovarian GCT patient [27]. Parental cell KGN and established clones derived from the same cell line were cultured at 37 °C and 5% CO₂ in DMEM medium (Dulbecco modified Eagle medium) supplemented with 10% bovine fetal serum (FBS) and 1% of penicillin/streptomycin. HEK-293 cell line (RRID:CVCL_M624; obtained from ATCC, #CRL-1573) was used to generate lentiviral particles. Culture medium was also DMEM, supplemented with FBS 10%. Cells grew at 37 °C and 5% CO₂. Cell lines were authenticated using STR DNA profiling and routinely tested for mycoplasma contamination.

2.2. Clone generation using CRISPR/Cas9 and genomic characterization

Single guides were designed to target the mutated allele of *FOXL2*, using Breaking Cas Design tool (<https://bioinfo.gp.cnb.csic.es/tools/breakingcas/>).

Guides sg1.3 and sg1.4 (Table 1) were cloned in the pLenti-sgRNA plasmid for virus generation and cell infection. Lentivirus containing spCas9 sequence or one of the two specific *FOXL2* C134W mutation guides (sg1.3 or sg1.4) were generated to infect KGN cell line. HEK-293 cells were seeded 24 h before transfection in medium lacking penicillin/streptomycin. For

transfection, either plasmid containing spCas9, or one of the two guides together with the second-generation packaging vectors, were mixed with lipotransfectin and added to the HEK-293 cells medium. Viruses from the different conditions were collected after 48- and 72-h post-transfection, centrifuged at 300 g for 10 min and viral supernatant was filtered with a 0.45 µm filter and stored at -80 °C. For infection, supernatant containing spCas9 lentivirus was mixed with 8 µg·mL⁻¹ polybrene, added to the KGN culture and incubated at 37 °C and 5% CO₂ for at least 6 h. After that time, fresh DMEM medium was added to the culture. Selection of cells containing Cas9 plasmid required the presence of 5 µg·mL⁻¹ of blasticidin in the medium for 13 days. The same infection protocol was used to infect KGN cells with lentiviral particles harboring sg1.3 or sg1.4 guides. In this case, 48 h postinfection, selection was done with 2 µg·mL⁻¹ of puromycin for 48 h. After completing antibiotic treatment, three different pools were generated (no guide, sg1.3, and sg1.4) and subsequently divided into two. One part of the culture was seeded, by serial dilution, in p96 well plates containing one cell per well to generate individual clones. The remaining part was kept as bulk culture (named as “pool”), which was used to study the activity and the specificity of the guides.

To determine CRISPR/Cas9 activity, DNA from pools and clones was isolated. Amplification of the sequence including the mutation site was performed by PCR using *FOXL2*-Fw and *FOXL2*-Rv primers and DNA polymerase. Sanger sequencing was carried out in the Genomic Unit of Instituto de Salud Carlos III (ISCIII) and then combined with the TIDE platform to determine the presence and magnitude of insertions and deletions present in the analyzed PCR products. To specifically determine the novel allelic variants, MiSeq DNA was performed on the target region PCR amplified with primers deepSeq *FOXL2*-Fw and deepSeq *FOXL2*-Rv (Table 1). The resultant PCR products were used for a second PCR to add specific indexes required for ulterior sample identification. FASTQ files comprising sequencing data were analyzed by CRISPResso. This platform analyzes the region closest to the Cas9 cut and compares the different insertions/deletions/substitutions found in the analyzed sample with a reference sequence.

A nucleofection strategy was also used to deliver the CRISPR/Cas9 machinery to the nucleus of the KGN cell line. Electroporator NEPA21 (Nepa Gene Co., Ltd., Chiba, Japan) was used to deliver pX458 plasmid containing specific guide RNAs and spCas9 endonuclease into KGN cells. After 48 h, positive GFP cells were sorted and grew in normal culture conditions.

Table 1. Resources used in this work.

Cell culture media	Primers and guides
<ul style="list-style-type: none"> DMEM (Dulbecco's modified Eagle's medium) high glucose/Invitrogen (Waltham, MA, USA) (#61965-026) FBS (fetal bovine serum) Tetracycline Negative/Capricorn Scientific (Ebsdorfergrund, Germany) (FBS-TET-12A) Penicillin/streptomycin/Lonza (Basel, Switzerland) (#DE17-602E) FBS (fetal bovine serum)/Sigma-Aldrich (St. Louis, MI, USA) (#F7524-500ML) Opti-MEM (Serum reduced medium)/Gibco Thermo Fisher Scientific (Waltham, MA, USA) (31985062) 96-well plates/Greiner bio-one (Les Ulis, France) (658986) µ-Slide 8 Well high/lbidi (Grafelfing, Germany) (80806) 	<ul style="list-style-type: none"> sgRNA1.3: 5'-CGAACAATGTTCTTCCAGGGCCGGG-3' sgRNA1.4: 5'-CTTCTCGAACAATGTTCTTCCAGG-3' deepSeq FOXL2-Fw: 5'-TTCGTCGGCAGCGTTCAGATGTGTATAAGAGACACCGAAAGTTCCCGTTCTACGAGAA-3' deepSeq FOXL2-Rv: 5'-GTCTCTGGCTCGGAGATGTGTATAAGAGACACCGAAAGTTGTGAGGAAAGCCAGACT-3' Primers for RT-qPCR assays: FOXL2-279F primer: 5'-GAATAAAGAAGGGCTGGCAAAAT-3'; FOXL2-WT-specific-reverse primer: 5'-CCTTCTCGAACAATGTTCTTCC-3' CD24-Fw: 5'-GGCCATTTTTCAGTCTGAG-3'; CD24-Rv: 5'-GATGCTGGGTGCTTGGAGAA-3' HOPX-Fw: 5'-TTTTCGAGGAGAGACCAG-3'; HOPX-Rv: 5'-CAGCTGGTTAAGCGGAGGA-3' CYP19A1-Fw: 5'-GATTCGGCAGCAAACTTGGG-3'; CYP19A1-Rv: 5'-TGACCAATACGAAACAAGGCCG-3' LOX-Fw: 5'-ATGATCACAGGTGCTGCTC-3'; LOX-Rv: 5'-GTGTTGGCATCAAGCGGTC-3' CXCR4-Fw: 5'-CATTCCTTTCCTTTCGAG-3'; CXCR4-Rv: 5'-ATCCATTTGCCCAATGCCCA-3' CAVI-Fw: 5'-AGGGCAACATCTACAAGCCC-3'; CAV1-Rv: 5'-GCCGTCAAACCTGTGTGTC-3' INHA-Fw: 5'-TCCCAAGCCATCTTTCCTCCAG-3'; INHA-Rv: 5'-TCACCTGGCGCTGCTGTAT-3' SKP2-Fw: 5'-GATGTGACTGGTCTGGTTGCTGT-3'; SKP2-Rv: 5'-GAGTTCGATAGGTCCATGTGCTG-3' BMPRI1A-Fw: 5'-CTTTTACCCTGAAGAAGCAGCT-3'; BMPRI1A-Rv: 5'-AGAGCTGAGTCCAGGAAACCCTGT-3' STAT3-Fw: 5'-ACCAGCAGTATAGCCGCTTC-3'; STAT3-Rv: 5'-GCCCAATCCGGGCAATCT-3' IL6-Fw: 5'-CCTGAACCTTCCAAAGATGGC-3'; IL6-Rv: 5'-TTCCAGGCAAGTCTCCTCA-3' SOX4-Fw: 5'-GACCTGCTGACCTGAAACC-3'; SOX4-Rv: 5'-CCGGGCTCGAAGTAAAAATCC-3' SOX9-Fw: 5'-AGGAAACGCATCAAGAC-3'; SOX9-Rv: 5'-CTGTAGGCGATCTGTGGGG-3' SMAD6-Fw: 5'-GCTACCAACTCCCTCATCACT-3'; SMAD6-Rv: 5'-CGTACACCCGCAATAGAGCGG-3'
Kits	Software and platforms
<ul style="list-style-type: none"> DNA polymerase/NZYTech (Lisbon, Portugal) (MB354) MiSeq DNA/Illumina (San Diego, CA, USA) (MS-102-2003) BCA system/Pierce (Waltham, MA, USA) (23227) ECL western blotting system/Thermo Fisher Scientific (Waltham, MA, USA) (32106) Click-IT Edu Imaging Kits/Thermo Fisher Scientific (Waltham, MA, USA) (C10337) Senescence b-Galactosidase Staining/Cell Signaling (Danvers, MA, USA) (#9860) Corning Matrigel Invasion Chamber 24-well plate 8.0 Micron/Corning (Bedford, MA, USA) (354480) RNase-Free DNase Set/Qiagen (Redwood City, CA) (79254) miRNeasy Mini Kit/Qiagen (Hilden, Germany) (1038703) TruSeq Stranded Total RNA/Illumina (San Diego, CA, USA) (20 020 596-20 020 599) TMT10plex Isobaric Label Reagents and Kits/Thermo Fisher Scientific (Waltham, MA, USA) (60110) miRNeasy Mini Kit/Qiagen (Hilden, Germany) (1038703) Agilent RNA 6000 Nano Kit/Agilent Technologies (Waldbronn, Germany) (5067-1511) High sensitivity DNA Chips/Agilent Technologies (Waldbronn, Germany) (5067-4626) 	<ul style="list-style-type: none"> SnapGene (RRID: SCR_015052) TIDE (https://hide.nki.nl) CRISPResso (http://crispresso2.pinelolab.org/submit) ImageJ (RRID:SCR_003070) GraphPad Prism (RRID: SCR_002798) Gene Set Enrichment Analysis software/Molecular Signatures Database (RRID: SCR_016863) Cytoscape (RRID: SCR_003032) Morpheus by Broad Institute (RRID: SCR_017386) (https://software.broadinstitute.org/morpheus/) VolcaNoseR (https://nuvgens.science.uva.nl/VolcaNoseR/) Connectivity Map 02 (RRID: SCR_015674)

Reagents and plasmids		
Hoechst 33324/Thermo Fisher Scientific (Waltham, MA, USA) (H3570)	pLenti-sgRNA/Addgene (Watertown, MA, USA) (#71409)	
Propidium iodide (PI)/Sigma-Aldrich (St. Louis, MI, USA) (P5318)	pAX2 and pMD2G (second generation lentiviral packaging vectors) and LV-H2BEGFP/Kindly provided by Dr. Amparo Cano	
BSA (bovine serum albumin)/Sigma-Aldrich (St. Louis, MI, USA) (#A7906)	Edit-R Inducible Lentiviral Cas9 (Revvity Dharmacon™, USA)	
Triton X-100/Sigma-Aldrich (St. Louis, MI, USA) (#X100-1L)	Lipofectamine/InvivoGen (San Diego, CA, USA) (ant-ipt-1); Blastocidin/InvivoGen (San Diego, CA, USA) (ant-bi-05)	
Prolong Gold with 40,6-Diamidino-2-Phenylindole (DAPI)/Cell Signaling Technology (Danvers, MA, USA) (P36935)	Polybrene/Sigma-Aldrich (St. Louis, MI, USA) (H9268)	
Paraformaldehyde/Sigma-Aldrich (St. Louis, MI, USA) (158127-5G)	TBS (Tris-buffered saline)/Canvax Biotech (Cordoba, Spain) (BR0042)	
Glycerol/Sigma-Aldrich (St. Louis, MI, USA) (G5516)	Criterion TGX Stain Free Precast Gels/Biorad (Hercules, California, USA) (5678084)	
Crystal violet/Sigma-Aldrich (St. Louis, MI, USA) (C6158)	RIPA buffer/Sigma-Aldrich (St. Louis, MI, USA) (R0278)	
Ketoconazole/Selleckchem (Cologne, Germany) (R41400)	Trizol (Invitrogen)/Thermo Fisher Scientific (Waltham, MA, USA) (15596-026)	
Dasatinib/Selleckchem (Cologne, Germany) (S7782); BRD6929/Selleckchem (Cologne, Germany) (E0391); Palbociclib/Selleckchem (Cologne, Germany) (S4482)	Transfer-Blot Turbo Transfer Pack/Biorad (Hercules, California, USA) (1704159)	
Ampure XP Beads/Beckman Coulter (Pasadena, CA, USA) (A63880)		
SuperScript III First Strand/Invitrogen (Waltham, MA, USA) (18080-051)		
qPCR SYBR™ Green Mix 8 (Applied Biosystems)/Thermo Fisher Scientific (Waltham, MA, USA) (4309155)		
Antibodies		
Name	Source	Working dilution
Anti-mouse α -tubulin	Sigma-Aldrich (St. Louis, MI, USA) (T9026)	1 : 5000
Anti-rabbit FOXL2	Sigma-Aldrich (St. Louis, MI, USA) (F0805)	1 : 1000
Anti-rabbit phospho-Akt (Ser473) D9E	Cell Signaling (Danvers, MA, USA) (#4060)	1 : 1000
Anti-mouse Akt (pan) 40D4	Cell Signaling (Danvers, MA, USA) (#2920)	1 : 1000
Anti-rabbit phospho-p44/42 MAPK Erk1/2 Thr202/Tyr204 D13.14.4E	Cell Signaling (Danvers, MA, USA) (#4370)	1 : 1000
Anti-rabbit p44/42 Mitogen-Activated Protein Kinase 1/3 (Erk1/2)-137F5	Cell Signaling (Danvers, MA, USA) (#4695)	1 : 1000
Anti-rabbit phospho-GSK-3 β (Ser9) (5B3)	Cell Signaling (Danvers, MA, USA) (#9323)	1 : 1000
Anti-rabbit GSK-3 β (27C10)	Cell Signaling (Danvers, MA, USA) (#9315)	1 : 1000
Purified Mouse Anti-p27 (Kip1)	BD Biosciences Pharmingen (Franklin Lakes, NJ, USA) (554069)	1 : 5000
Anti-rabbit phospho-Smad2/3 (Ser 423/425)	Santa Cruz Biotechnology (Dallas, TX, USA) (sc-11769R)	1 : 200
Anti-mouse Smad2/3 (C-8)	Santa Cruz Biotechnology (Dallas, TX, USA) (sc-133 098)	1 : 1000
HRP-labeled anti-mouse secondary antibody	GE Healthcare (Chicago, IL, USA) (NA931-1ML)	1 : 5000
HRP-labeled anti-rabbit secondary antibody	GE Healthcare (Chicago, IL, USA) (NA934-1ML)	1 : 5000

Clone generation and genomic studies were performed as previously described.

2.3. Western blot analysis and proteomic study

Protein extraction and SDS-PAGE were performed according to standard protocols. Briefly, cells were lysed by RadioImmunoPrecipitation Assay (RIPA) buffer (150 mM NaCl, 0.1% SDS, 50 mM Tris-HCL) (pH 7.5), 0.5% sodium deoxycholate, 1% nonyl phenoxypolyethoxyethanol (NP-40) supplemented with protease and phosphatase inhibitors followed by protein dissociation using an ultrasonic processor UPH100H (Hielscher, Teltow, Germany) with 3 pulses of 5 s. Samples were centrifuged at 16873 *g* at 4 °C for 15 min and protein concentration was quantified following the BCA assay. Protein separation, transfer, antibody incubation, blocking and ECL detection were performed as indicated in Martin et al. [28]. Primary and secondary antibodies are detailed in Table 1.

Individual cell protein extracts (10 µg) were used for the TMT 10-plex quantitative proteomics analyses (see previous works for full protocol [29,30]). TMT experiments were analyzed on an Orbitrap Exploris 480 mass spectrometer (Thermo Fisher Scientific, Waltham, MA, USA) equipped with the FAIMS Pro Duo interface (Thermo Fisher Scientific, Waltham, MA, USA). Peptide separation was performed on the Vanquish Neo UHPLC System (Thermo Fisher Scientific, Waltham, MA, USA) using established protocols [29]. MS data were analyzed with MaxQuant (version 2.1.3, Max Planck Institute of Biochemistry, Planegg, Germany) using standardized workflows. Mass spectra *.raw files were searched against the Uniprot UP000005640_9606.fasta Homo sapiens (human) 2022 database (20 577 protein entries) using reporter ion MS2 type for TMTs. Data normalization and data analysis was performed according to established protocols [29,31]. Proteins identified with one or more unique peptides, $\pm 1.5 \log_2$ foldchange values, and an adjusted *P*-value ≤ 0.05 were selected as statistically significant dysregulated proteins. Cut-offs were selected according to previous [29,30,32]. Analysis of the results was completed by GSEA and manual clusterization using Cytoscape (including EnrichmentMap and AutoAnnotate).

2.4. RNA extraction and transcriptomic characterization

RNA processing involved TRIzol-based isolation method followed by DNase I treatment in all the cases. Sample quality was tested on an Agilent Bioanalyzer 2100 Eukaryote Total RNA nano assay. A

whole-transcriptomic study was conducted by preparing total RNA libraries, as specified in the TruSeq Stranded Total RNA manufacturer instructions. Next steps involved pooling the samples in equimolar concentrations for sequencing on the NextSeq 500 instrument, preceded by various quality tests using the Agilent Bioanalyzer 2100 High Sensitivity DNA kit. Data obtained was analyzed by the Bioinformatic Unit of our center applying the same statistical parameters as in the proteomic study: $\pm 1.5 \log_2$ foldchange and *P*_{adj} < 0.05. Enrichment in gene ontology (GO) terms was conducted using preranked [33] GSEA software and network representation of enriched terms was obtained using enrichmentMap and AutoAnnotate from Cytoscape. Heatmaps and unsupervised clustering of top differentially expressed genes was generated using Morpheus and Volcano plots using VolcanoR.

For validation studies of the transcriptomic results, same RNA samples were subjected to RT-qPCR using SYBR green PCR master mix in the StepOne Real-Time PCR system and the appropriated primers (Table 1).

For the specific amplification of wild type and c.402C>G *FOXL2* alleles, we used the primers and conditions described by Shin et al. [34] (Table 1).

2.5. Cell growth, senescence, cell cycle migration, and drug sensitivity

Cytell Cell Imaging System (GE Healthcare Life Sciences, Marlborough, MA, USA) was used as a digital microscope and cell counter in all the cell growth assays carried out along the study. For these experiments, 1500 cells from each clone were seeded in 96 well black glass bottom plates and maintained in culture under normal CO₂ (5%) and temperature (37 °C) conditions. At selected time points, cells were stained with 1 µg·mL⁻¹ Hoechst and 10 µg·mL⁻¹ of propidium iodide for 15–30 min at 37 °C. Cell viability was assessed using BioApp for image acquisition, and the generated data was analyzed using GRAPHPAD software.

To analyze kinetic aspects of mitotic cell division, cells were previously infected with lentiviral particles expressing Histone 2B fused to green fluorescent protein and then seeded in a six well glass bottom plate. Images were captured every 10 min for 48 h by fluorescence microscopy.

Drug sensitivity assays were performed using THUNDER Imager Live Cell & 3D Cell Culture & 3D Assay imaging system (Leica-Microsystems, Wetzlar, Germany). Cells treated with different concentrations of ketoconazole, dasatinib, palbociclib and BRD6929 for 48 h, were stained with Hoestch and

propidium iodide (the same concentrations as above) and images of each experimental condition were taken to establish cell number and death rates. Drug reconstitution and dilution were carried out following data-sheet instructions. Drug eligibility was based on previous published works [12,35,36] and Cmap (Connectivity Map, Broad Institute) results derived from our transcriptomic and proteomic studies. Data of differentially expressed genes (DEGs) with a $\pm 1.5 \log_2$ foldchange and a $P_{adj} < 0.05$ and differentially expressed proteins (DEPs) with a $\pm 1.25 \log_2$ foldchange and a $P_{adj} < 0.05$ were compared and the resulting common genes were then inputted into the Cmap platform for further analysis. Finally, palbociclib and BRD6929 were selected among the three major categories from a list of 100 drug candidates grouped by different description/activity features.

Senescence was determined using β -Galactosidase staining. A total of 70,000 cells per clone were seeded in six well transparent plates. Two days later, when cell confluency reached 60–70%, cells were fixed and stained following manufacturer's recommendations (Senescence β -galactosidase Staining kit from Cell Signaling, Danvers, MA, USA). After cell staining, a total of 11 images comprising every part of the well were taken using Leica DM IL LED inverted Laboratory Microscope with the 10 \times objective and the Leica MC170 HD Microscope camera. Quantification was done by IMAGEJ software and results were represented as the percentage of cells exhibiting a positive β -galactosidase staining pattern.

Flow cytometry cell cycle analyses were performed on cells previously trypsinized, fixed with cold 70% ethanol and resuspended in PBS-T (PBS + 0.03% TritonX-100). Fixed cells were treated with RNase ($0.5 \mu\text{g}\cdot\text{mL}^{-1}$) and then DNA was stained with $1 \mu\text{g}\cdot\text{mL}^{-1}$ Propidium iodide. DNA profile data were retrieved using a FACSCantoII and analyzed using Floreada.io (<https://floreada.io/analysis>).

An EdU incorporation assay was carried out to determine the percentage of cells that were at S-phase. Cells were seeded in glass cover slips placed in six well transparent plates. After reaching 50% confluency, EdU was added to the medium at a final concentration of 10 μM . One hour later, we proceeded to perform Edu and nuclei staining according to manufacturer's instructions. EdU labeling was detected by fluorescent microscopy (Leica-Microsystems, Wetzlar, Germany) employing 10 \times and 20 \times objectives (N PLAN 10 \times /0.25 DRY and HC PL FLUOTAR 20 \times /0.55 DRY). The percentage of positive EdU cells were determined by IMAGEJ software.

The invasive capacity was analyzed by a Transwell invasion assay as described in Martin et al. [28], with

minimal modifications. In brief, once 2000 cells were seeded in low serum conditions in the upper part of the chamber, we waited for 48 h before removing Matrigel from the lower membrane where cells are attracted by the 10% serum containing media placed in the bottom well. Next, cells were fixed and stained with 1% glutaraldehyde and 0.5% crystal violet, respectively. Images were taken with a Leica MC170 HD Microscope camera coupled with a Leica DM IL LED inverted Laboratory Microscope at 10 \times magnification. Number of invasive cells was determined by IMAGEJ software.

2.6. Zebrafish care and handling. Xenograft assays and image analysis

Zebrafish adult fish (*Danio rerio*, wild type) were crossed to obtain zebrafish embryos. Adult zebrafish were kept in aquaria with a ratio of one fish per liter of water, a day/night cycle of 14:10 h and water temperature of 28.5 °C was constantly maintained, according to the published protocols [37]. Procedures used in the experiments, fish care and treatment were performed in agreement with the Animal Care and Use Committee of the University of Santiago de Compostela and the standard protocols of Spain (Directive 2012-63-DaUE). At the end of the experiments, the embryos used were euthanized by tricaine overdose. Adult zebrafish are derived from AB/Tuebingen line and maintained in our facilities (ES270280346401; AE-LU-003). Animal license number 01/20/LU-003 was approved by Xunta de Galicia for the animal experiments included in this work.

Zebrafish embryos were collected at 0hpf (hours postfertilization) and incubated at 28.5 °C in petri dishes until 48 hpf. Then, KGN cells were trypsinized and concentrated in an Eppendorf at a rate of ≈ 1 million cells for each condition and resuspended in 10 μL of PBS (phosphate-buffered saline) with 2% of PVP (polyvinylpyrrolidone) to avoid cellular aggregation. After cell preparation, 48 hpf embryos were anesthetized with 0.003% of tricaine (Sigma, St. Louis, MI, USA) and injected with the corresponding clones. Cell injection was performed using borosilicate needles (1 mm O.D. \times 0.75 mm I.D.; World Precision Instruments, Sarasota, FL, USA). Between 100 and 200 cells were injected into the circulation of each fish (Duct of Cuvier) using a microinjector (IM-31 Electric Microinjector, Narishige) with an output pressure of 20 kPa and 15 ms of injection time per injection. Afterwards, embryos were incubated until 6 days postinjection (dpi) at 34 °C in 30 mL Petri dishes with SDTW (Salt Dechlorinate Tap Water). Imaging of the injected

embryos were performed using a fluorescence stereomicroscope (AZ-100; Nikon Europe, Amstelveen, The Netherlands) at 1, 4, and 6 dpi to measure the spreading and proliferation of the injected cells in the caudal hematopoietic tissue (CHT) of the zebrafish embryos. To perform the analysis of the acquired images at the different time points Quantifish software [38] was used. This software processes all the images and performs the measure of the fluorescence intensity and area of positive pixels, corresponding to the cells injected, above a certain threshold. With these parameters, integrated density is obtained allowing the researcher to compare different times between images and obtain a proliferation ratio of the cells in the region of the CHT of the embryos, where the cells normally metastasize. As a measure of the metastatic capacity of the injected cells, the number of tumors present in the tails of the embryos were scored. Tumor counts were determined based on the size of the tumor and the separation between the cell clusters inside the tail of the fish.

2.7. Statistical analyses

GRAPHPAD software was used to perform statistical analysis of all the data. ANOVA test and Student's *t*-test were used to compare edited clones to their reference controls (PARENTAL cells) with a confidence interval of 95%.

3. Results

3.1. Precise disruption of FOXL2 c.402C>G, p.C134W mutation via CRISPR/SpCas9 genome editing system

To study the role of FOXL2-C134W mutation in tumor maintenance, an allele-specific gene editing approach based on CRISPR technology was developed, to selectively target the mutant allele without affecting its corresponding wild-type counterpart. This last aspect is especially relevant since the indiscriminate destruction of both alleles might cause side effects. We hypothesized that the FOXL2 c.402C>G, p.C134W allele could be specifically inactivated by exploiting the fact that this pathogenic missense mutation gives rise to a nucleotide variation in the seed sequence (one to five nucleotides upstream of the PAM) that potentially affect SpCas9 recognition. Following this strategy, we designed two allele-specific sgRNA, sg1.3 and sg1.4, that include the c.402C>G mutation at position +7 and +2, respectively, upstream of the PAM (Fig. 1a). The specificity of these guides was assayed in KGN cells, the only commercially

available cell line derived from an ovarian granulosa human tumor that harbors the FOXL2 c.402C>G mutation in heterozygosity. As described in Fig. 1b, CRISPR machinery was sequentially introduced in the target cells by lentiviral infection resulting in three pool cell populations expressing Cas9 alone or in combination with sg1.3 or sg1.4 small guide RNAs.

Subsequent genomic analysis by deep amplicon sequencing allowed us to potentially distinguish between five different allelic variants (Fig. 1c). Two, non-edited, consist of the wild type and mutant alleles (referred as 402C and 402G, respectively). The other two are the modified wild type and mutant alleles containing several types of insertions and deletions (designated as Indels-402C and Indels-402G, respectively). In a fifth category (named as others), we could not identify which of the two alleles had been edited. As expected, we only detected, at approximately 50% frequency, wild type (402C) and mutant (402G) alleles in the pool expressing the SpCas9 alone (KGN-Cas9) (Fig. 1c; Table S1). Importantly, the co-expression of Cas9 with any of the two sgRNAs caused a dramatic reduction in the representation of the mutant, 402G allele. In the case of the sg1.3 guide, we could only detect 3.44% of the intact 402G allele, while the guide sg1.4 was associated with the presence of just 8.83% 402G reads. As expected, this reduction of 402G alleles was accompanied by a corresponding increase of Indel-402G alleles, which were detected in 25.04% and 14.31% of the reads from the sg1.3- and sg1.4-infected cells, respectively. Additional modifications (others) were also identified in 10.27% and 3.02% of the reads from the corresponding sg1.3- and sg1.4-infected cells. It is interesting to note, the increase of intact, wild type reads detected in sg1.3- and sg1.4-infected cells when compared with the control, KGN-Cas9 ones (61.24% and 73.85%, respectively, vs 50.21%). Finally, a specific pattern of indels is detected in a sgRNA-dependent manner. While the most common indel in the pool containing sg1.3 is the deletion of a cytosine in position 399, the insertion of an adenine between positions 403 and 404 is the most frequent indel promoted in the case of sg1.4 (Table S2). Similar results were obtained when the CRISPR complexes were introduced in KGN cells by nucleofection (Fig. S1).

In conclusion, although a complete absence of genomic edition in the wild type allele could not be unambiguously demonstrated, the inability to identify the presence of genetic modifications, unlike in the case of the mutant, 402G allele, underlines the selectivity of both sg1.3 and sg1.4 guides toward the Cas9-dependent disruption of the mutated FOXL2 allele.

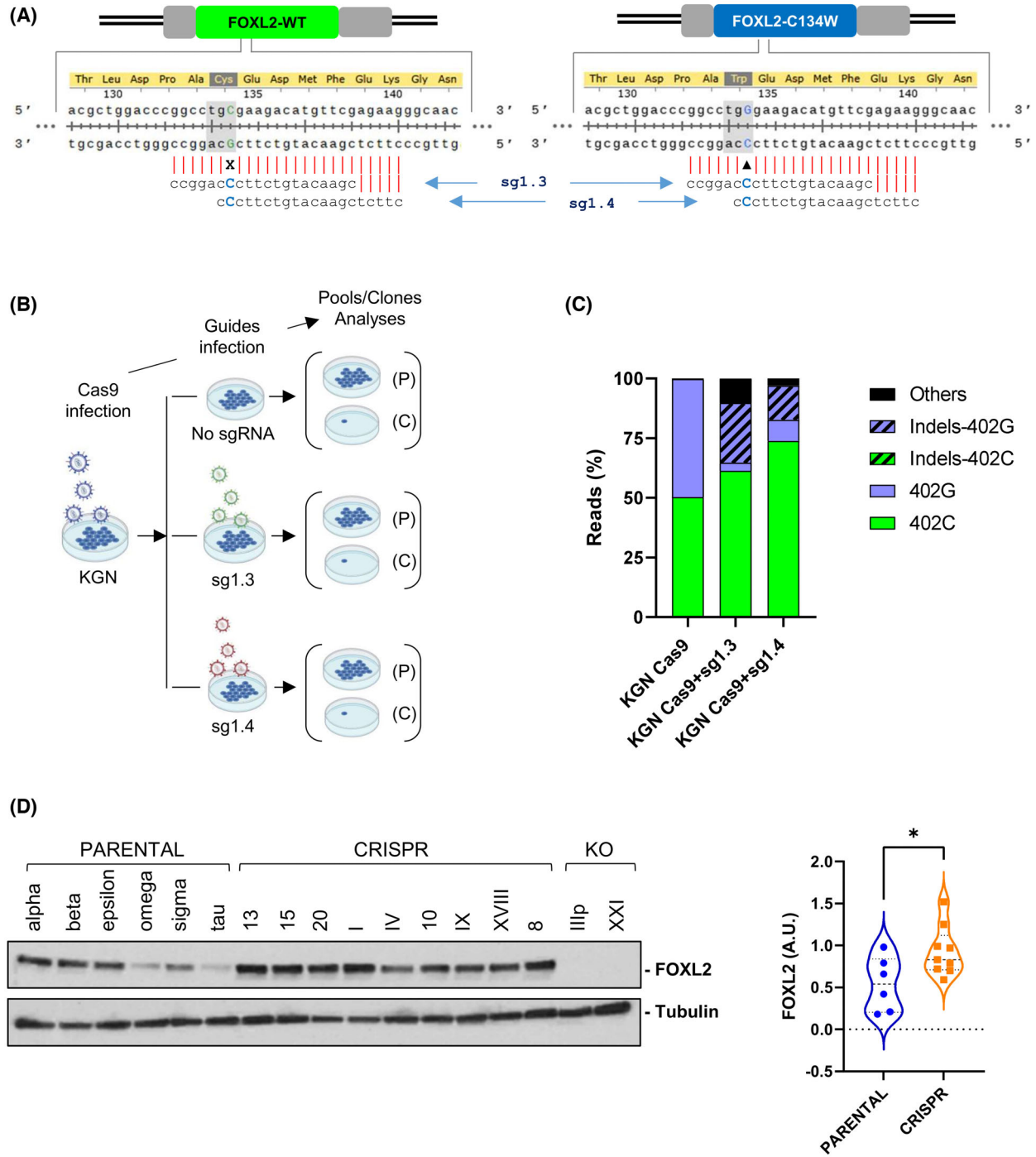


Fig. 1. Editing of *FOXL2* c.402C>G mutation in KGN cells. (A) Scheme for *FOXL2* c.402C>G sgRNA location. *FOXL2* wild type and mutant alleles are represented along with the corresponding amino acid sequences for both alleles. Mutant and wild type bases are highlighted in blue and green, respectively. Guides designed specifically to target mutant allele are represented below each allele. (B) Timeline for the generation of pools (P) and clones (C). Each round of infection is followed by a selection performed with antibiotics (Blasticidin and Puromycin, respectively). (C) Guide specificity on the *FOXL2* c.402C>G mutant allele. Graph represents percentage of reads, obtained from a single experiment, matching each edited and not edited alleles for the pool of cells generated upon infection with Cas9, Cas9 + sg1.3 and Cas9 + sg1.4. (D) *FOXL2* protein expression in PARENTAL, CRISPR, and KO clones isolated in this study. Violin graph shows the quantification of *FOXL2* expression in PARENTAL ($n = 6$) and CRISPR ($n = 9$) clones. The mean \pm SD is represented by dashed lines within the violin plots. Results were compared using one-tailed, unpaired Student's *t*-test ($*P < 0.05$).

To further analyze the consequences of CRISPR-mediated elimination of the *FOXL2* c.402C>G mutation, we isolated and characterized individual clones from the pools transfected with the different CRISPR complexes. A total of 37 clones obtained by a single cell cloning approach were characterized by sequencing. As expected, all the 10 clones derived from the cell pool that was transfected with SpCas9 without sgRNAs, are identical to the original KGN cells (data not shown), which means that they preserve an intact *FOXL2* mutation in heterozygosity. These PARENTAL clones were identified with Greek letters and will be used as controls for later analyses. Remarkably, the majority of the remaining clones (25 out of the 27 isolated from pools co-expressing SpCas9 and either of the two allele-specific sgRNAs, hereafter referred as CRISPR clones) showed some type of CRISPR activity on the mutant allele (Table S3). Most of those cases (21 out of 25) displayed Indel events that exclusively occurred on the mutant allele with frame shift modifications leading to premature stop codons (Table S3). The observed Indel pattern was like the one already detected in the pools, single cytosine deletion at position 399 in the case of the sg1.3 clones and a prevalent adenine insertion between nucleotides 403 and 404 for the sg1.4 ones (Table S3). The guide origin of the clones is reflected in their nomenclature with Arabic and Roman numbers to designate clones coming from sg1.3 and sg1.4, respectively. Although small insertions or deletions are the major causes of allele-specific inactivation (77.8%), we failed to detect the presence of the mutant allele in a small percentage of clones (4 out of 27, 14.8%), indicating that a large deletion occurred at the mutant allele or, alternatively but less probable, DNA correction by homology-directed repair took place in the cell using the wild type allele on the homologous chromosome as a template. These four clones were also included in the CRISPR group due to their identical behavior to the CRISPR clones (Fig. S2). Finally, two knockout (KO) clones (IIIp and XXI) harbor indels in both alleles that provoke changes in the open reading frame that result in truncated, and presumably nonfunctional, wild type and mutant proteins (Table S3). Therefore, this finding suggests that, although to a much lesser extent, biallelic modification by CRISPR can also occur in our experimental system. These two clones were excluded from the CRISPR group due to significant differences in certain features, such as their transcriptomic profiles (Fig. S2).

To complete the molecular characterization of these clones, we analyzed by western blot the impact of CRISPR-mediated genome edition of *FOXL2* on its

protein expression. Interestingly, while *FOXL2* levels were completely abrogated in the two KO clones, CRISPR clones showed a significant *FOXL2* upregulation compared to PARENTAL, KGN controls (Fig. 1d). Moreover, specific analysis of wild type *FOXL2* mRNA by RT-qPCR, revealed a clear increase when mutant allele is selectively inactivated (Fig. 1d). Notably, over-expression of the edited mutant allele, encoding a dysfunctional *FOXL2* protein, was also observed in CRISPR clones when this allele was detectable by RT-qPCR amplification (Fig. S3). These findings suggest the presence of a transcriptional repression mechanism associated with the *FOXL2*-C134W mutation.

In conclusion, we have generated a CRISPR-mediated system that allows us to specifically eliminate the *FOXL2* c.402C>G allele in KGN granulosa tumor cells. Moreover, the abrogation of the *FOXL2*-C134W mutant restores wild type function of *FOXL2* as a transcription factor.

3.2. *In vitro* targeted disruption of *FOXL2* c.402C>G allele diminishes cell proliferation of AGCT derived cells

We investigated whether specific cleavage of *FOXL2* c.402C>G mutant allele mediated by CRISPR could induce cellular changes by comparing at different levels PARENTAL and CRISPR clones. In the first set of experiments, we conducted viability assays of PARENTAL and CRISPR clones. Results show that proliferation capacity of edited cells was diminished compared to non-edited controls (Fig. 2a). In the same experiments, cell death levels were not able to explain this antiproliferative phenotype since no significant differences were detected between CRISPR and PARENTAL clones (Fig. 2b). Interestingly, in a close to significance way, the percentage of senescent cells was increased among CRISPR clones when compared with the PARENTAL ones (Fig. 2c). We then further assessed the cell cycle of both clonal populations by flow cytometry analysis. As shown in Fig. 2d and Fig. S4, CRISPR clones show significantly higher levels of G1 cells and lower percentages of S and G2/M cells, which reflects a lower cell cycle rate for the clones in which the *FOXL2* c.402C>G allele has been eliminated using CRISPR. Moreover, we found a reduced capacity of sg1.3- and sg1.4-targeted cells to incorporate EdU which indicates a potential delay in S-phase entry and/or retarded progression (Fig. 2e). Next, we performed time-lapse microscopy analysis to monitor in more detail cell cycle kinetics by imaging for 48 h H2B-EGFP expressing cells of both

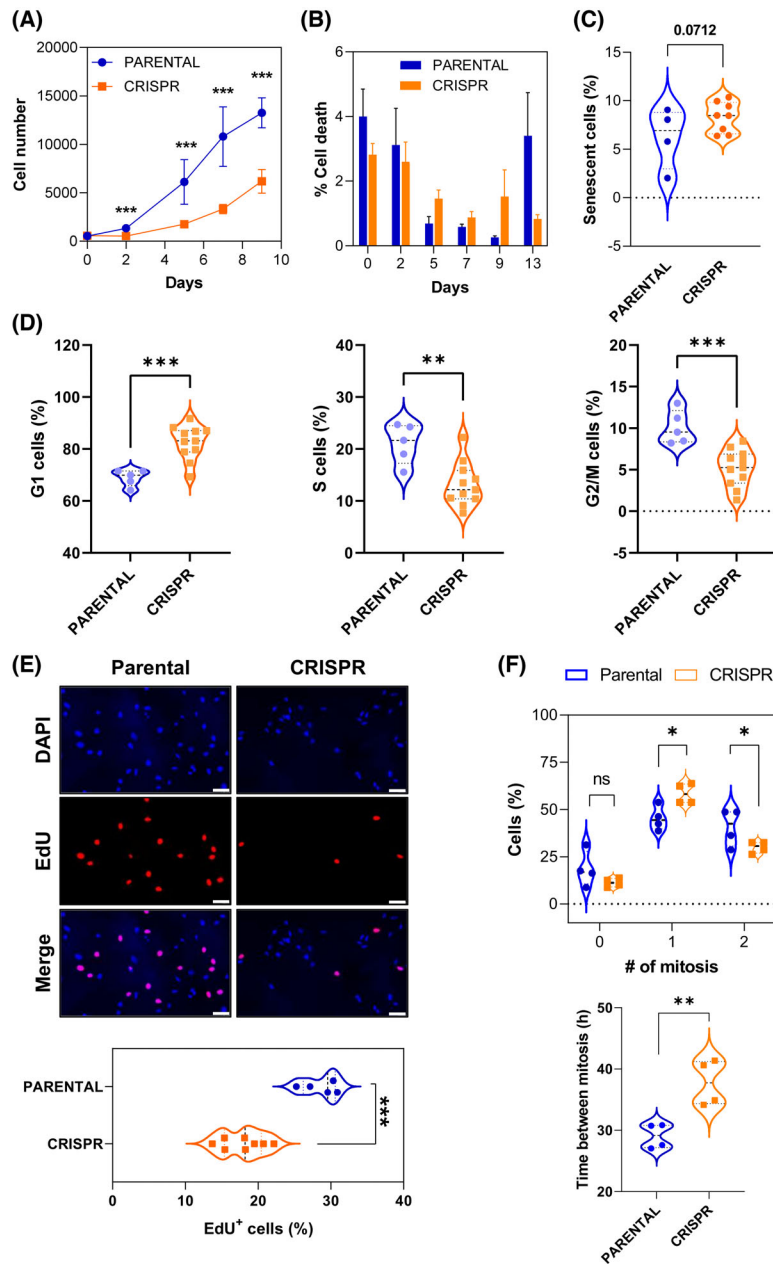


Fig. 2. Specific *FOXL2* c.402C>G mutation elimination causes a decrease in cell growth. (A) Growth curve experiment for PARENTAL ($n = 5$) and CRISPR ($n = 9$) clones. Each data point represents the mean of three technical replicates, with error bars indicating the standard deviation (SD). Representative graph of two experimental replicates. (B) Graph shows the percentage \pm SD of cell death related to each day of the same experiment showed in panel (A). No significant differences were found between the different groups at each time point. (C) Graph represents mean of percentage of positive cells for β -galactosidase staining in PARENTAL ($n = 4$) and CRISPR ($n = 8$) clones. A close-to-significance P -value was obtained when PARENTAL and CRISPR clones were compared. (D) Cell cycle profiling by propidium iodide staining of PARENTAL ($n = 5$) and CRISPR ($n = 11$) clones. Violin graphs show the percentage of cells found in G1, S, and G2/M phases. (E) Cell proliferation in PARENTAL ($n = 5$) and CRISPR ($n = 8$) clones estimated by incorporation of EdU. The upper panel corresponds to representative clone images from both groups, showing EdU incorporation (red, middle images) and all nuclei (blue, upper images). Scale Bar = 50 μ m. The bottom graph shows percentage of cells positive for EdU staining in the nucleus. (F) CRISPR clones show modifications in cell cycle timing. The upper graph shows the percentage of cells that undergo 0, 1, or 2 rounds of mitosis for 48 h. The bottom violin graph shows the quantification of the time lapse between two subsequent mitoses in CRISPR and PARENTAL clones. In all the violin plots, the mean \pm SD is represented by dashed lines. In all the experiments of this figure, data was compared with one-tailed, unpaired Student's t -test (ns: non-significant; * $P < 0.05$; ** $P < 0.01$; *** $P < 0.001$).

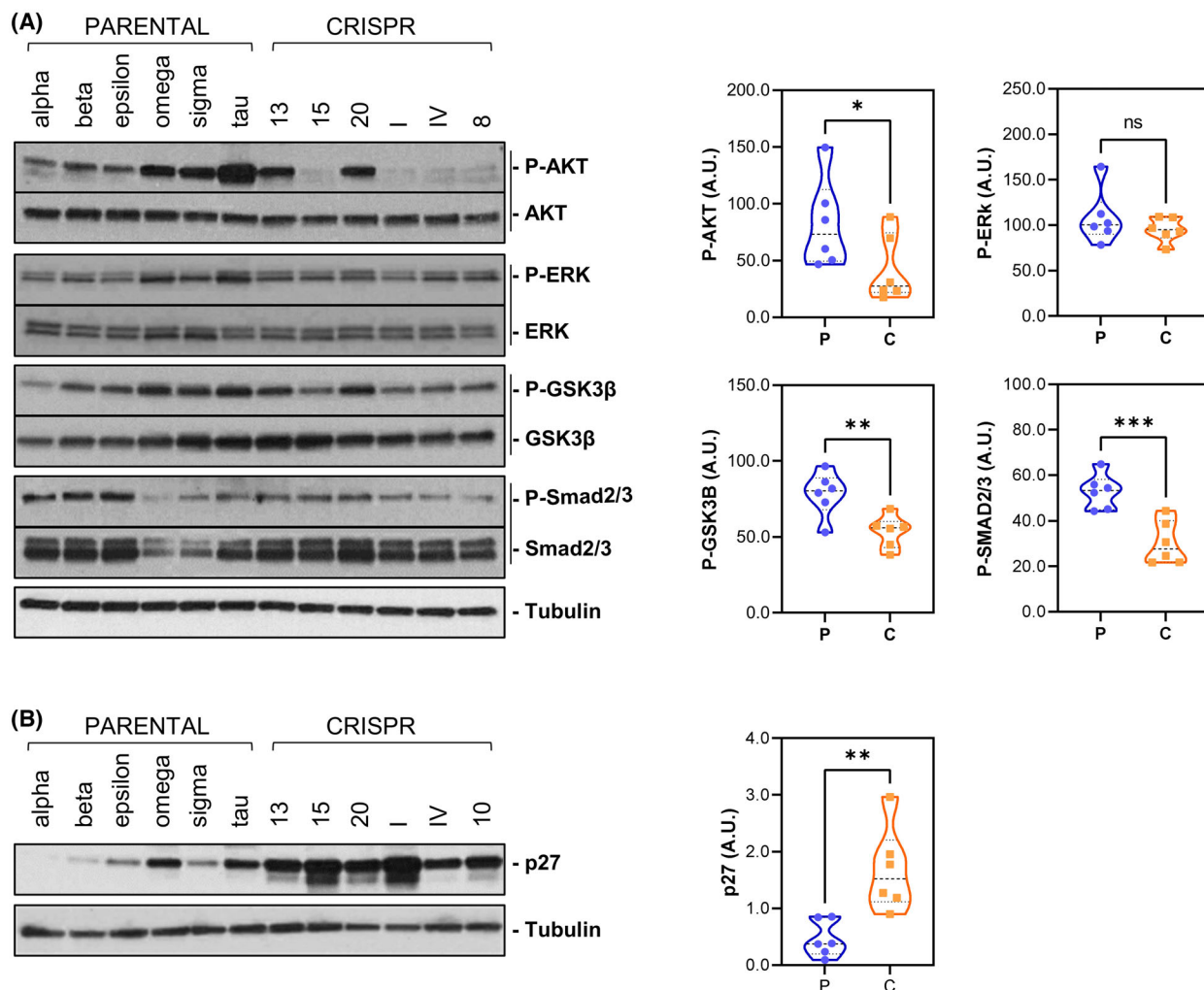


Fig. 3. Cell survival and growth regulation pathways are affected by the specific elimination of *FOXL2* c.402C>G mutation in KGN cells. Protein expression of molecules involved in proliferative pathways (A) and p27 (B). Six different PARENTAL and CRISPR clones are analyzed. Right graphs show quantification of the expression results shown in (A) and in (B) for PARENTAL (P) and CRISPR (C) clones. Each phospho-protein was normalized with its total protein expression and the expression of tubulin. Proteins in B were normalized with tubulin protein levels. In all the violin plots, the mean \pm SD is represented by dashed lines. Results were compared using one-tailed, unpaired Student's *t*-test (ns, non-significant; **P* < 0.05; ***P* < 0.01; ****P* < 0.001).

genotypes. Data indicate that, although no differences were detected for the percentage of cells that do not undergo mitosis, most CRISPR cells tend to divide only once, whereas a great fraction of PARENTAL cells exhibit two rounds of cell division in the same period (Fig. 2f). Confirming these results, CRISPR clones needed significantly more time to go from one mitosis to the next one than the PARENTAL ones (38 ± 4 h vs 29 ± 2 h).

To try to decipher the molecular mechanism responsible for this reduced proliferative ability associated with *FOXL2*-C134W inactivation, different signaling pathways involved in the regulation of cell survival

and proliferation were analyzed. While no differences were observed in terms of ERK1/2 proteins, phosphorylation of AKT, GSK3 β , and Smad2/3 was significantly reduced in CRISPR clones (Fig. 3a). Interestingly, this phenomenon was accompanied by a significant increase of p27 (Fig. 3b), a *FOXL2* regulated player [39,40] involved in cell cycle inhibition whose expression is known to be also negatively controlled by PI3K pathway [41].

Altogether, these data let us conclude that specific abrogation of *FOXL2* C134W mutation negatively impacts on cell proliferation by causing a deceleration in the cell cycle and a moderate increase in senescence.

These changes in cell fate are associated to inhibition of PI3K/AKT and TGF β -Smad2/3 pathways as well as the concomitant upregulation of the cell cycle inhibitor p27.

3.3. Specific elimination of mutated FOXL2 allele attenuates cell migration both *in vitro* and *in vivo* and predispose to a better response to drug therapies

Most of the AGCT clinical cases do not exceed stage I at the time of diagnosis and have good prognosis. However, a small percentage of these patients can relapse, showing metastatic lesions in different locations that correlate with poor survival rates [42,43]. Thus, we aimed to analyze the invasive potential of both clonal groups by standard transwell analysis. We seeded the cells on top of the filter membrane of the transwell insert and exposed the cells to a chemo-attractant that was added on the bottom part of the well. Forty-eight hours later, as shown in Fig. 4a, CRISPR clones showed less invasive capacity than the PARENTAL ones, indicating that this malignant feature was also diminished upon the elimination of the FOXL2 c.402C>G mutation.

Considering that *in vivo* studies in zebrafish have been reported to faithfully determine the metastatic potential of a broad range of cancer cells [44], two clones per each FOXL2 genotype were injected into the circulation of 48 h-postfertilization embryos and incubated at 34 °C for 6 days. The number of micro-metastasis was quantified in the embryo tails by taking images at 1, 4, and 6 days postinjection as a measurement of the spread and metastatic capacity of FOXL2 targeted and non-targeted KGN cells. As illustrated in Fig. 4b, a significant reduction of around 50% in tumor burden was scored when CRISPR clones were injected compared to PARENTAL ones, suggesting an important role of the FOXL2 C134W mutation in the dissemination ability of AGCT-derived cells.

Although treatment of AGCTs is mainly based in surgery and platinum-based combinations, a progressive characterization of these tumors along the years has allowed to introduce and propose new therapeutic approaches. The senolytic dasatinib and the CYP17 inhibitor ketoconazole are among these alternatives. Dasatinib has shown a synergistic effect when used with chemotherapy in AGCTs [34]. On the other hand, inhibition of CYP17 has been proposed as a promising therapeutic option for AGCT [12] because FOXL2 c.402C>G mutation leads to overexpression of this key regulator of steroidogenesis [45]. In fact, ketoconazole, a CYP17 inhibitor, has shown activity in advanced

AGCT in clinical and *in vitro* studies [36]. Therefore, we decided to study the activity of these two compounds in a contest of CRISPR-mediated elimination of the FOXL2 c.402C>G mutation. As shown in Fig. 4c, cell growth is significantly inhibited in both PARENTAL and CRISPR clones treated with either dasatinib or ketoconazole. Notably, this inhibitory effect was significantly stronger in CRISPR clones compared to PARENTAL clones when treated with dasatinib (1 μ M), resulting in a 48% vs 23% reduction, respectively ($P < 0.05$). Similarly, cell death increased in both clone types at the highest doses of dasatinib and ketoconazole (Fig. 4d). Interestingly, the average fold induction of cell death relative to untreated cells was higher in CRISPR than in PARENTAL clones for both the highest dose treatments of dasatinib (5.3 vs 2.6) and ketoconazole (11.7 vs 4.4), with P values approaching significance ($P = 0.06$ and $P = 0.08$, respectively).

3.4. Elimination of FOXL2 c.402C>G mutation modifies the transcriptomic expression signature of granulosa tumor cells

It has been previously described that mutation 402C>G in FOXL2 transcription factor, due to its location in the DNA-binding domain, affects the expression of several target genes [26], changing the transcriptomic profile of granulosa cells. It has been demonstrated, both *in vitro* and *in vivo*, that these alterations affect pathways related with TGF β signaling, ECM organization, ovarian infertility genes, regulation of gene expression by several interleukins, FSH apoptosis, cholesterol, and prostaglandin biosynthesis and regulation [46,47]. To gain insights into the transcriptional effects of eliminating the 402C>G mutation of FOXL2 in KGN cells, we compared the expression signatures of CRISPR clones ($n = 3$) versus those of the PARENTAL ones ($n = 4$). Principal component analysis (PCA) (Fig. 5a) of the different clones in the experiment revealed a clear separation between the PARENTAL and CRISPR clones, defining them as distinct entities. Differentially expressed genes (DEG; fold change >1.5 or <1.5 and adjusted P -value of <0.05) in PARENTAL clones, when compared with CRISPR counterparts, include a total of 710 upregulated and 943 downregulated transcripts (Fig. 5b; Table S4). These results were validated by RT-qPCR of a selected group of DEGs (Fig. S5).

Most of the top-50 most up/downregulated DEGs (Fig. 5c) have been previously related with cancer at some extent (Table S5). Some of them (CAV1, CAV2, and KSR1) are involved in MAPK signaling, whereas

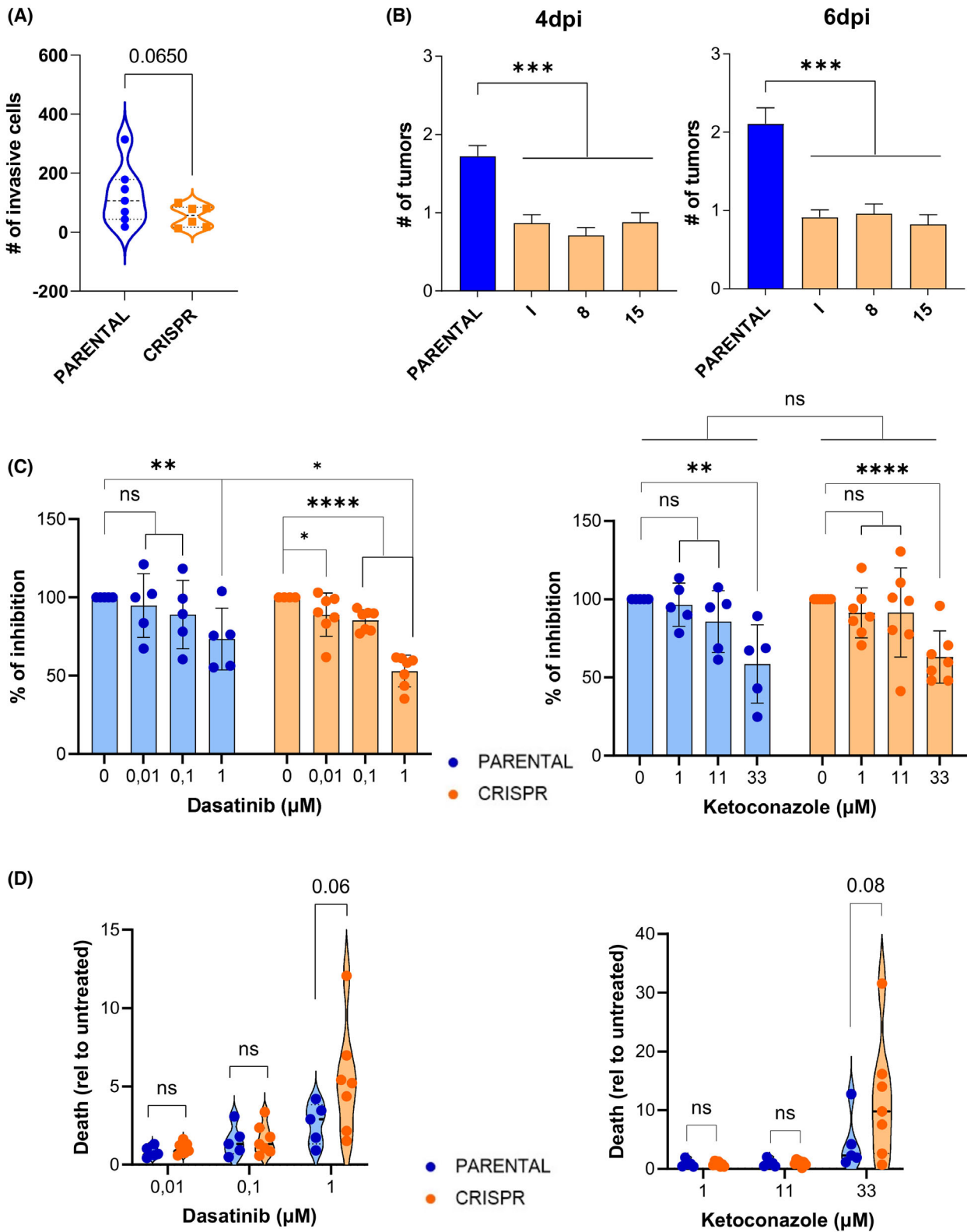


Fig. 4. Migration capacity and sensitivity to dasatinib and ketoconazole is altered in CRISPR clones. (A) *In vitro* migration assay. Violin plots show all the clones individually analyzed for the experiment, 48 h after seeding cells in transwells. A close-to-significance increase in the average number of invasive cells is found among CRISPR ($n = 6$) clones when compared to PARENTAL ($n = 7$) ones. (B) *In vivo* migration assay in zebrafish. Graphs represent the number of tumors counted in animal tail. PARENTAL clones ($n = 3$) are unified in a single (blue) column while three CRISPR clones (orange and identified as "1," "8," and "15") are shown individually. Statistical differences are observed at 4 and 6 days post cells injection (4 dpi and 6 dpi, respectively), revealing a reduction in tumor formation in CRISPR clones. (C) Effect of CRISPR-mediated elimination of FOXL2 c.402C>G mutation on KGN cell following treatment with dasatinib (left) and ketoconazole (right). Graphs show the percentage of cells detected with different doses of the drugs 48 h after treatment starts. Each cell count value was normalized to the number of cells in control wells (0 μM drug concentration), set as 100%. (D) Cell death was also measured 48 h post-treatment with dasatinib (left) and ketoconazole (right). Fold induction of cell death, relative to untreated cells, is shown for the different drug dose. At the highest drug doses, cell death levels were higher in CRISPR clones compared to PARENTAL clones, approaching statistical significance. In panels C and D, data are from five PARENTAL and seven CRISPR clones. In all the violin plots, the mean \pm SD is represented by dashed lines. Error bars indicate standard error of mean (SEM) in B and \pm SD in C. In A, C, and D, results were compared using one-tailed, unpaired Student's *t*-test. In B, data were compared using ordinary one-way ANOVA with Tukey multiple comparisons test. ns, non-significant; * $P < 0.05$; ** $P < 0.01$; *** $P < 0.001$; **** $P < 0.0001$.

others have been associated with TGF β signaling (LOX, TSKU), extracellular functions/junctions (JCAD, COL4A5, and CDH12) and apoptosis (BMF), among other cellular features. It is noteworthy that PDL1 (CD274) ranks among the top 25 most upregulated genes in clones harboring the C134W mutation. This upregulation could potentially promote immune response evasion, thereby facilitating tumor growth. However, overexpression of PDL1 in FOXL2 C134W tumors might render these tumors more sensitive to anti-PDL1 therapy. Furthermore, 50% of the top-50 most up/downregulated DEGs have already been associated with granulosa cells and/or FOXL2 (Fig. 5c; Table S5). Hence, CSPG4, JPH2 and TAGLN have also been found upregulated in TGF β -induced GCTs, when compared with wild type granulosa cells [48]. On the other hand, among the most significantly downregulated genes, CDH12 and CD55 are granulosa cell markers [49,50], whereas CYP11A1, a FOXL2 target gene [51], plays a crucial role in steroid hormone synthesis in granulosa cells [52].

To further explore the potential roles of the DEGs, enrichment of GO terms was analyzed using GSEA. As shown in Fig. 5d, up-regulated genes in PARENTAL versus CRISPR clones were enriched in GO gene sets related to cell cycle, including DNA replication and repair, spindle pole, mitosis and centromere condensation. These results correlate with the differences observed between the two clone groups in terms of cell proliferation and mitosis progression and duration (Fig. 2). Upregulated genes were also significantly enriched in pathways related to protein synthesis and post-translational modifications like sumoylation (data not shown). Further, several gene sets related to estrogen metabolism, a critical function of granulosa cells [53,54] where FOXL2 have been previously implicated [25,55], were downregulated in

C134W cells compared to wild type CRISPR clones (Fig. 5e,f).

All this transcriptomic information indicates that the CRISPR-mediated elimination of the C134W mutation leads to the acquisition of a different cellular status. To explore more of this new condition, we decided to compare the transcriptomic profile of our PARENTAL and CRISPR clones with that generated previously by Weis-Banke and coworkers for human granulosa cells expressing different amounts and types of exogenous FOXL2 variants [26]. A hierarchical cluster analysis shows that CRISPR clones grouped close to human normal granulosa cells transfected with either empty, FOXL2-wt or FOXL2-C134W expression vectors, whereas PARENTAL clones cluster closer to the KGN cells used by Weis-Banke et al. [26] (Fig. S6). These results indicate a potential reversion of KGN cells to their wild-type origin upon elimination of the C134W mutation.

3.5. Protein expression signature of KGN cells is significantly altered upon the elimination of FOXL2 c.402C>G mutation and can be used to discover molecules with growth inhibitory activity against AGCT cells

To gain further insights in the expression profile associated with the lack of FOXL2-C134W mutation, we carried out a proteomic study comparing PARENTAL and CRISPR clones. Mirroring the transcriptomic results, two very differentiated groups appear upon PCA examination (Fig. 6a). To identify DEPs, we filter our results by an adjusted *P*-value of <0.05 and a fold change beyond ± 1.5 . Using these parameters, we detected a total of 29 downregulated and 60 upregulated proteins in PARENTAL clones when compared with the CRISPR group (Fig. 6b; Table S6).

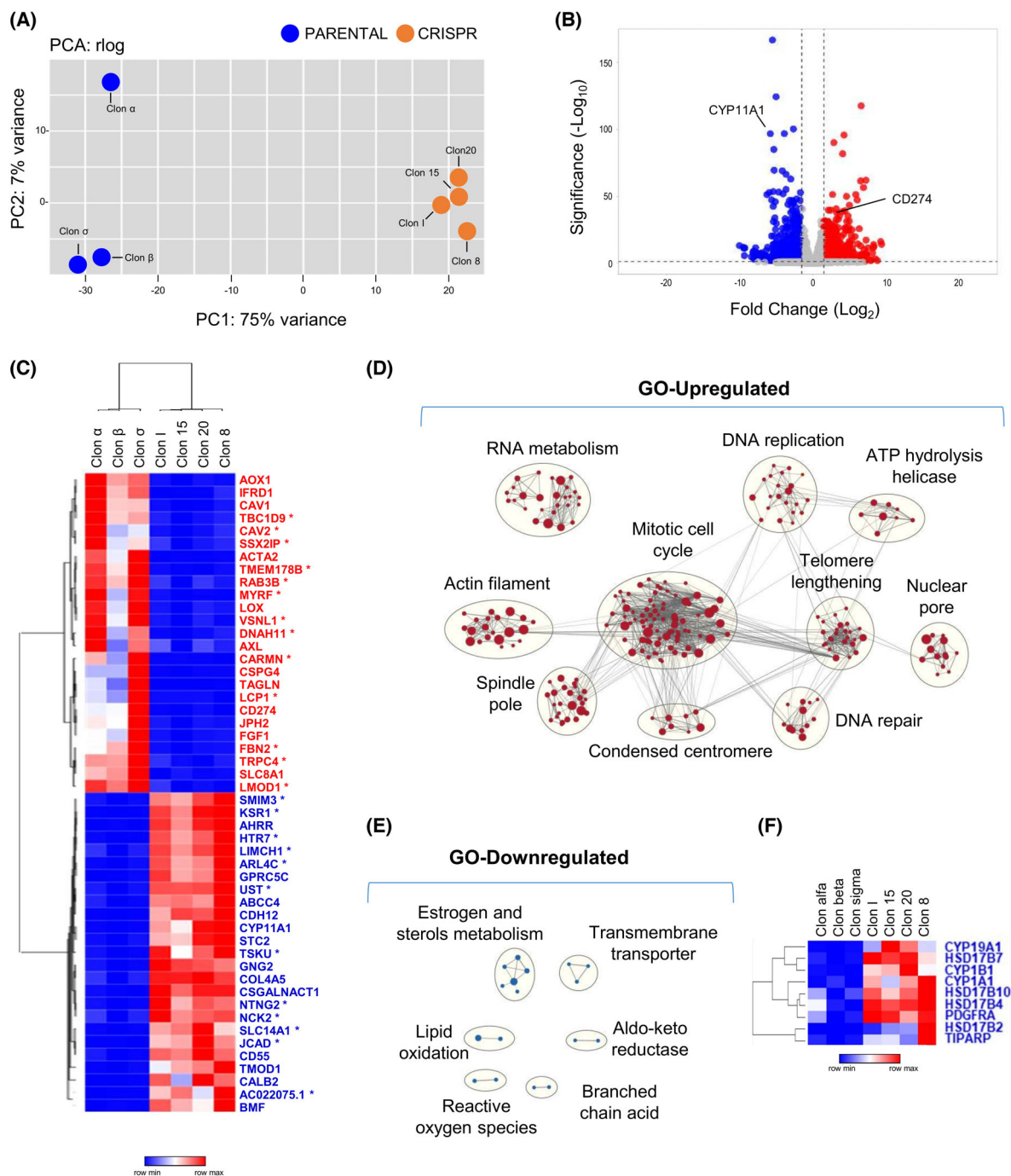


Fig. 5. CRISPR-mediated elimination of *FOXL2* c.402C>G mutation induces significant changes in the transcriptomic profile of granulosa tumor cells. (A) Principal component analysis of RNAseq data from PARENTAL (blue, $n = 3$) and CRISPR (orange, $n = 4$) clones. (B) Volcano plot for differential gene expression in *FOXL2* C134W (PARENTAL, $n = 3$) vs edited (CRISPR, $n = 4$) clones. Downregulated genes with adjusted P -value < 0.05 and \log_2 of fold change lower than -1.5 are depicted in blue. Upregulated genes with adjusted P -value < 0.05 and \log_2 of fold change higher than 1.5 are depicted in red. (C) Heatmap showing an unsupervised clustering of top-25, upregulated and downregulated genes according to adjusted P -value. Genes that have not been previously related to granulosa cells are marked with an asterisk. (D) Clusters of GO gene sets differentially enriched in genes upregulated in PARENTAL versus CRISPR clones at q -value < 0.05 . Node size is proportional to the number of genes identified in each gene set. The light gray edges indicate gene overlap between gene sets. (E) Clusters of GO terms at P -value < 0.05 enriched in downregulated genes depicted as in D. (F) Heatmap of genes belonging to the GOBP (Gene Ontology Biological Process) estrogen metabolic process significantly downregulated in KGN clones at adjusted P -value > 0.05 .

A significant fraction of these proteins was also found de-regulated in the transcriptomic study (Fig. 6c). Hence, 8 out of the 29 (27.6%) down-regulated proteins and 36 out of the 60 (65.6%) up-regulated ones were also differentially expressed at the RNA level (Table S7). Interestingly, a very good correlation was observed between RNA and protein expression of these 44 genes (Fig. 6c). Likewise for the transcriptomic results, the top-50 most up/down DEPs clustered the two clone types, CRISPR and PARENTAL, as two differentiated entities (Fig. 6d). Most of these top-50 DEPs have already been associated with cancer processes and more than half of them (30 out of 50) have been related to granulosa cell function and/or FOXL2 (Table S8). Interestingly, eight out of the top-50 DEPs were also found in the RNA-DEGs top-50 list (Fig. 6b,d). The up-regulated ones include TAGLN, an actin-associated protein related with cytoskeleton organization; LMOD1, which is involved in follicle maturation; CSPG4, a regulator of cell-substratum interactions; and CAV1 and CAV2, which are main components of the cavolae plasma membranes.

Regarding the three commonly down-regulated, top-50 DEGs/DEPs, CALB2 plays a key role in calcium-mediated signaling, SLC14A1 is a mediator of urea transport and CYP11A1 is a cytochrome P450 monooxygenase that catalyzes the side-chain hydroxylation and cleavage of cholesterol to pregnenolone, the precursor of most steroid hormones.

A GO analysis was also carried out with the DEPs found when PARENTAL clones were compared with CRISPR ones. For both up-regulated and down-regulated proteins, the GO terms detected significantly differed from the ones observed in the transcriptomic analyses (Fig. S7). GO-upregulated terms included “adhesion and extracellular structure,” “mitochondrial translation complex,” and “cholesterol metabolic regulation” among others, whereas “Pyrimidine ribonucleotide biosynthesis,” “Toll receptor signaling,” and “Multivesicular body” are among the GO-downregulated ones. It is interesting to note that GO terms common for both the transcriptomic and proteomic GO analyses were only detected for up-regulated genes and are mostly associated with ribosomes (Fig. 6e).

In a final step of our work, we tried to identify compounds that can induce the same expression signature that characterizes CRISPR clones when compared to the PARENTAL ones. To identify such compounds, we used the commonly downregulated genes from our transcriptomic and proteomic analyses (Fig. 7a) to interrogate the Connetivity Map (cMap) data base.

This platform allows to search for similarities to a given expression signature among expression signatures induced in nine cancer cell lines by more than 5000 small molecules [56]. This *in silico* approach allowed us to rank these drugs according to cMap connectivity scores (CS) that predicts the similarity of the profile induced by each compound with the interrogated expression profile (Table S9). Confirming the therapeutic value of this bioinformatic tool, ketoconazole, an orphan drug used for the treatment of AGCT [12] ranks #59 among the list of compounds. Since the top-100 drugs were enriched in Histone deacetylase (HDAC), Topoisomerase and CDK inhibitors (Table S10), we selected one HDAC inhibitor (Merck60 or BRD6929, ranked #63) and a CDK inhibitor (palbociclib, #17 of the ranking list) to study their activity on PARENTAL cells. As shown in Fig. 7b, BRD6929 induced cell death at its highest tested dose (1 μ M), achieving a 2.3-fold increase relative to untreated cells ($P < 0.01$). In contrast, as expected based on its mechanism of action, palbociclib had no effect on apoptosis induction. However, palbociclib was highly effective in inhibiting cell growth at all tested doses (0.01, 0.1, and 1 μ M), resulting in 85.52%, 54.72%, and 51.10% of cell numbers compared to untreated controls, respectively (Fig. 7c). Similarly, BRD6929 significantly reduced cell numbers at both 0.1 and 1 μ M, resulting in 86.74% and 64.50% of the values seen in untreated cells (Fig. 7c). Notably, weaker but non-significant effects were observed in CRISPR-edited clones treated with the same compounds (Fig. S8), suggesting a potential trend for higher activity on granulosa tumor cells carrying the FOXL2-C134W mutation.

In summary, the proteomic analysis of CRISPR and PARENTAL clones has allowed us to improve the results obtained at the transcriptomic level. The filtered results have produced a more detailed characterization of the PARENTAL clones and conducted us to find compounds, whose action partially mimic the elimination of the FOXL2-C134W mutation in KGN cells.

4. Discussion

4.1. Using CRISPR to study the role of FOXL2-C134W in granulosa cell tumors

The pathognomonic mutation c.402C>G is found in the *FOXL2* gene in over 95% of GTCs [13]. Since only a few other mutations have been reported in this tumor type [57], they can be considered a highly unique cancer primarily associated with a single

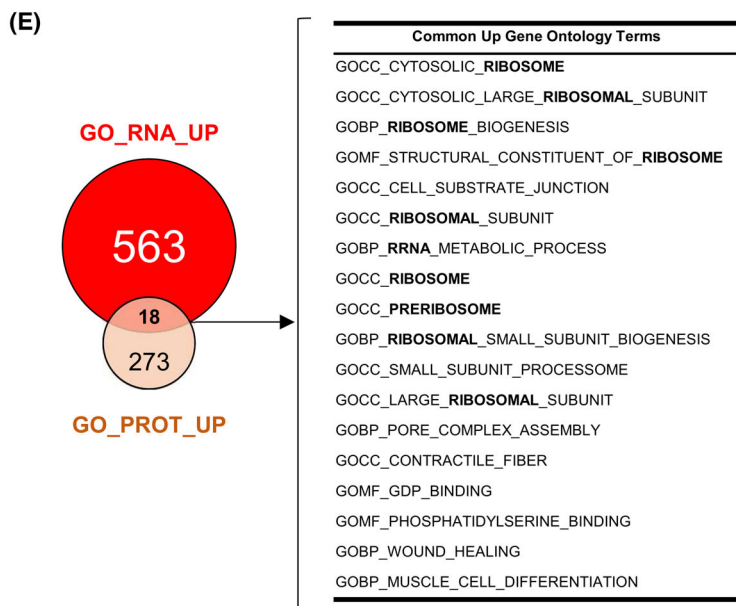
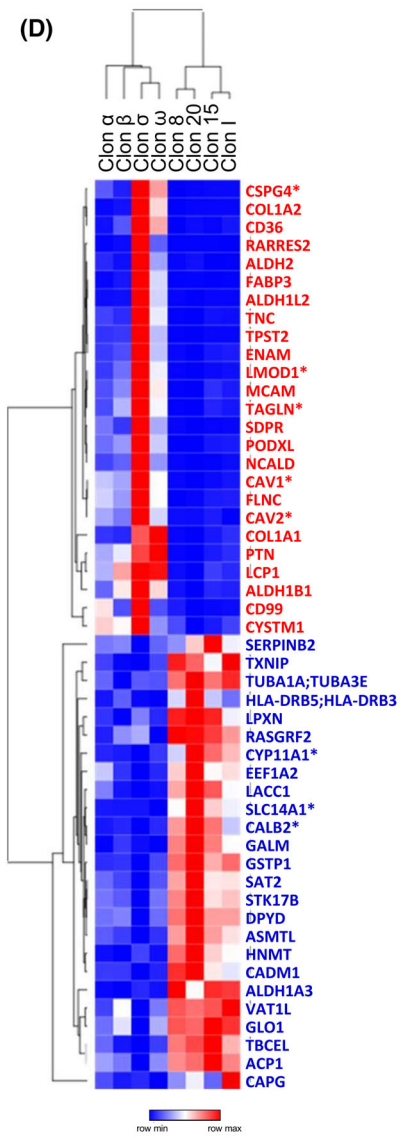
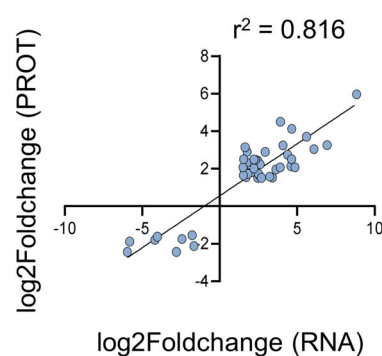
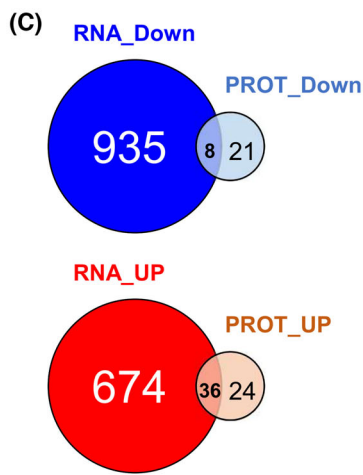
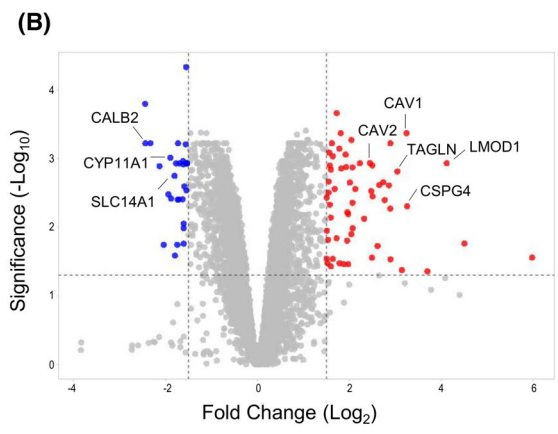
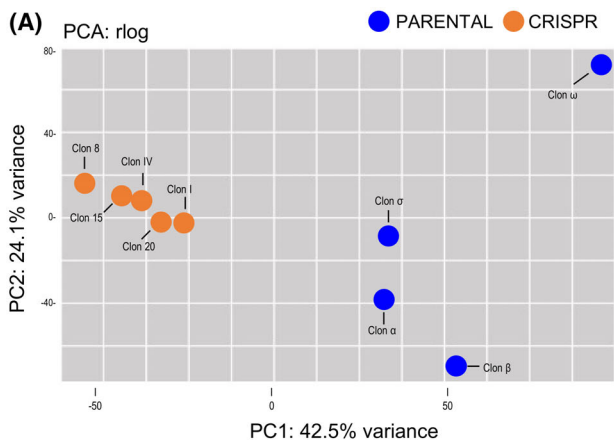


Fig. 6. Proteomic changes induced by the CRISPR-mediated elimination of *FOXL2* c.402C>G mutation. (A) Principal component analysis of protein data from KGN (blue, $n = 4$) and CRISPR (orange, $n = 5$) clones. (B) Volcano plot for differential gene expression in FOXL2 C134W (PARENTAL, $n = 4$) versus edited (CRISPR, $n = 5$) clones. Downregulated proteins with adjusted P -value < 0.05 and \log_2 of fold change lower than -1.5 are depicted in blue. Upregulated genes with adjusted P -value < 0.05 and \log_2 of fold change higher than 1.5 are depicted in red. (C) Venn-diagrams show the overlap of significantly de-regulated genes at the RNA and protein levels. The right plot shows the correlation between the RNA and protein fold change values of the common cases. (D) Heatmap of unsupervised clustering of the top-25, upregulated and downregulated proteins according to adjusted P -value. Genes that are also in the top-50, de-regulated list of the transcriptomic analysis are marked with an asterisk and indicated in panel B. (E) Venn diagram shows the GO terms at P -value < 0.05 enriched in upregulated genes. Common GO terms are also listed in the adjacent right table.

mutation in a single gene crucial for its cellular origin, the granulosa cells. Recently, the causal relationship between FOXL2-C134W and AGCTs has been demonstrated through the generation and characterization of a mouse model carrying the equivalent mutation in mice, *Foxl2* C130W [47]. All female mice carrying this mutation develop ovarian cancers that closely resemble AGCT pathology. We have reached similar conclusions by concurrently developing an equivalent mouse model (Amarilla-Quintana et al., unpublished results).

In this study, we utilized CRISPR technology to target and eliminate the *FOXL2* c.402C>G p.C134W mutation in KGN cells. By using mutation-specific guides, we demonstrated that the lack of FOXL2-C134W expression leads to a reduction in the malignant properties of these AGCT cells, indicating their partial dependence on the expression of this variant. This is not the first time CRISPR technology has been employed to target *FOXL2* in granulosa tumor cells. Tang and colleagues generated a FOXL2 null clone using CRISPR-mediated techniques [58]. In this clone, abnormal expression of two FOXL2 targets (StAR and CYP19A) was observed, along with decreased cell proliferation. In our study, we generated and analyzed 10 clones in which the *FOXL2* c.402C>G mutant allele was eliminated using Cas9 complexes, while the wild-type allele remained mostly unaffected by CRISPR activity. The resulting clones behaved similarly to the clone reported by Tang et al., with no major changes observed in apoptosis levels, although significant proliferative inhibition was induced. Additionally, our analysis revealed increased senescence in CRISPR clones compared to control clones. Furthermore, these KGN cells in which the FOXL2 C134W mutation was disrupted exhibited limited invasion capacity both *in vitro* and *in vivo* (see Fig. 4).

In a more recent study, Heman and colleagues [59] utilized CRISPR technology to revert the mutant allele to the wild-type one. The two wild-type, edited clones they obtained were extensively characterized at the transcriptomic level. Interestingly, they compared their signature profiles with those from FOXL2 null backgrounds and concluded that the FOXL2+/C134W

abnormalities are consistent with a gain-of-function scenario. Our results on FOXL2 expression in CRISPR clones confirm the gain-of-function role of the FOXL2 C134W mutation, suggesting it may exert an inhibitory effect on its transcription factor activity.

4.2. An expression signature associated with the FOXL2-C134W mutation

The expression studies conducted in this work have enabled us to characterize the expression signature associated with the presence of the FOXL2-C134W mutation in KGN cells. Transcriptional comparison of PARENTAL (nonedited) and CRISPR (edited) KGN clones indicates that the mutation is primarily associated with the upregulation of cell cycle division genes and the downregulation of estrogen regulators, consistent with a higher proliferative status and a lack of functions related to wild-type, differentiated granulosa cells. Similar transcriptomic analyses have been conducted by others using different approaches. Rosario and colleagues, after overexpressing wild-type and mutant FOXL2 in COV434 cells and silencing mutant FOXL2 expression in KGN cells, demonstrated that many genes regulated by mutant FOXL2 are involved in cell death, proliferation, tumorigenesis, and TGF- β signaling [46]. Years later, Weis-Banke and colleagues reported a transcriptional signature associated with FOXL2-C134W overexpression in human granulosa cells, characterized by epithelial-to-mesenchymal transition and induction of various cytokines, oncogenes, and factors involved in stemness [26]. More recently, Herman and colleagues analyzed the transcriptional consequences of reverting the FOXL2-C134W mutation to wild type and described dysregulated pathways, highlighting the TGF-beta pathway, cell adhesion, and migration processes as the most significantly disrupted [59]. Although there is no major conservation between the differentially expressed genes (DEGs) of all these studies and ours, the enriched terms and pathways are common among them. Indeed, our study also detected enrichment of TGF-beta, stemness, cell adhesion, extracellular matrix, epithelial-to-mesenchymal

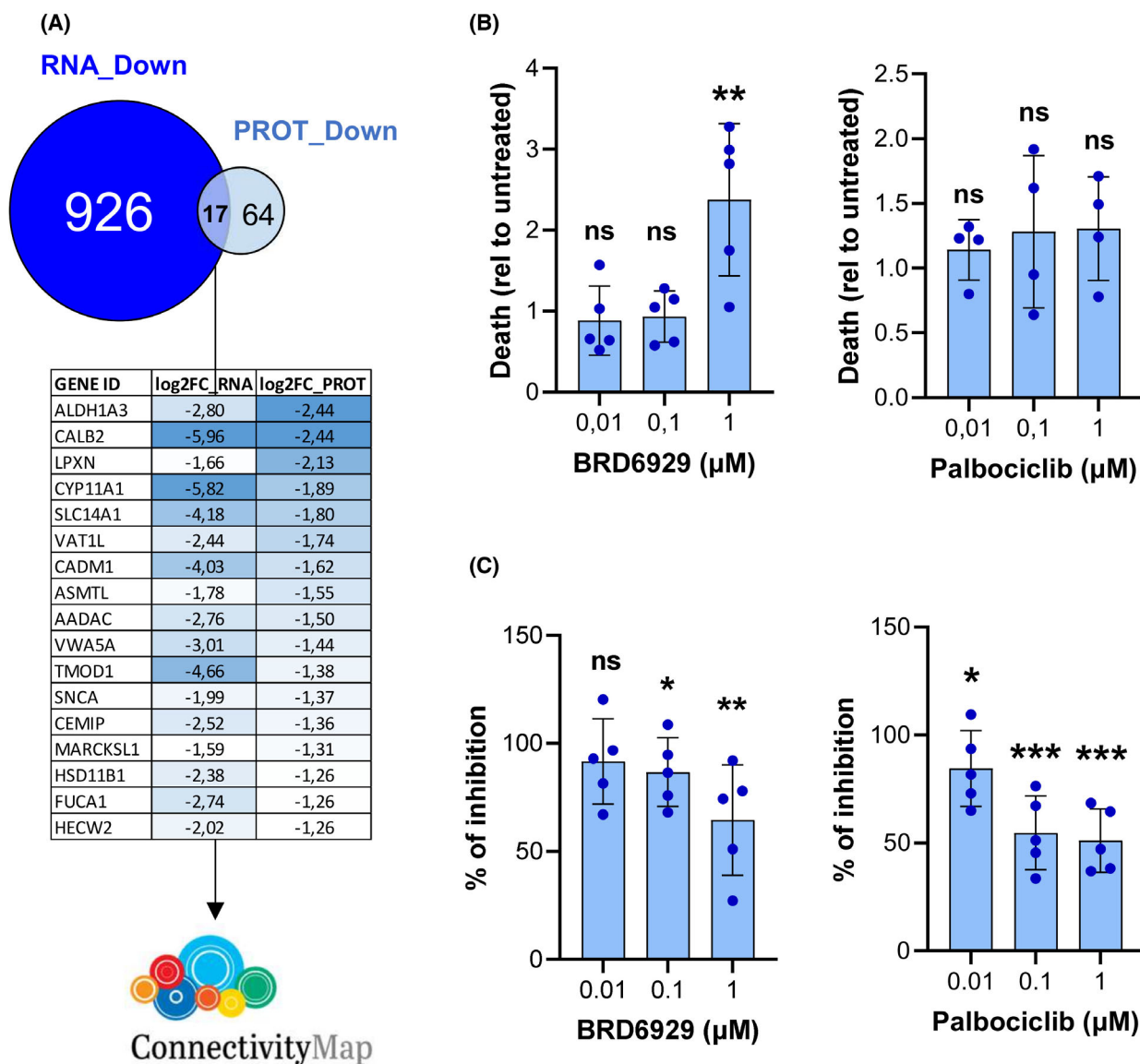


Fig. 7. Palbociclib and BRD6929 are two compounds identified with ConnectivityMap that recapitulate in KGN cells the antiproliferative effects induced by the elimination of FOXL2-C134W mutation. (A) Genes differentially downregulated in both the transcriptomic and proteomic analyses when comparing PARENTAL and CRISPR clones. Table shows the fold change downregulation of the 17 common genes. (B) Quantification of cell death in PARENTAL clones treated with varying concentrations of palbociclib ($n = 4$) and BRD6929 ($n = 5$), measured 24 h post-treatment. (C) Significant reductions in cell numbers were observed in PARENTAL cells ($n = 5$ clones) 48 h following treatment with palbociclib and BRD6929. In panels B and C, data represent results from treated PARENTAL clones, normalized to values from untreated clones. Error bars indicate \pm SD. In B and C, results were compared using one-tailed, unpaired Student's t -test. ns, non-significant; * $P < 0.05$; ** $P < 0.01$; *** $P < 0.001$; **** $P < 0.0001$.

transition, apoptosis, and migration among the significant outcomes obtained from Oncosignature, Terms, Pathways, or Perturbations sets (Tables S4 and S6).

To our knowledge, this is the first study in which transcriptomic and proteomic data are simultaneously obtained and analyzed for granulosa tumor cells. Fewer DEPs than DEGs were found in this work. This

could be due to the lower power of detection associated with proteomic methodology compared to transcriptomics. However, it is also possible that fewer proteins than transcripts are significantly altered due to post-translational mechanisms that further regulate the transcriptional changes induced by the FOXL2-C134W mutant form. Nevertheless, the differences

found between transcriptomic and proteomic data suggest that RNA perturbations should be interpreted with caution even in the study of a transcription factor such as FOXL2. On the other hand, the common deregulated genes and GO terms found between transcriptomic and proteomic studies are of particular value. Some of them have not been previously associated with AGCT, thus opening new avenues for understanding and treating the disease. Additionally, the common GO terms could be of special interest from a therapeutic point of view, as ribosome biogenesis appears to be a key and distinct upregulated feature among AGCT cells. Accumulated recent evidence highlights the importance of ribosome biogenesis in cancer [60], suggesting that further studies should be implemented to explore the potential of targeting ribosome biogenesis in AGCT.

4.3. Therapeutic implications: Improving existing approaches and finding new compounds for the treatment of AGCT

One of the main questions we initially posed in this study was whether CRISPR could serve as a therapeutic tool against AGCT. Our results strongly suggest so. By disrupting the *FOXL2* c.402C>G p.C134W mutation using CRISPR/Cas9, we observed a significant reduction in the malignant properties of KGN cells both *in vitro* and *in vivo*. Moreover, KGN cells in which the FOXL2-C134W mutation was eliminated became more susceptible to drugs previously used against AGCT, such as dasatinib and ketoconazole.

Our expression studies have provided valuable insights that could help the design of future therapeutic strategies. Notably, the higher levels of PDL1 (CD274) in KGN cells compared to those in the edited clones (Fig. 5c), suggest the potential clinical benefit of immune checkpoint-based therapies. Additionally, it is noteworthy that two HLA proteins (HLA-DRB3 and HLA-DRB5) were among the top-25 most downregulated proteins in KGN cells (see Fig. 6d). Although these proteins have not yet been implicated in immunotherapy, they could potentially impact the effectiveness of such treatments in AGCT.

Furthermore, employing an *in silico* approach, we utilized the signature induced upon the elimination of FOXL2-C134W in KGN cells to identify new compounds specifically targeting them. Remarkably, a fraction (16 out of 100) of the compounds identified through this strategy, overlapped with those reported in a previous drug screening conducted by others [35] (Table S9), aiming to uncover new therapeutic opportunities. In our study, HDAC inhibitors,

topoisomerase inhibitors, and CDK inhibitors emerged as the most promising categories for future therapeutic strategies, either as single agents or in combination with others.

5. Conclusions

The major limitation of this work is the fact that all experiments were conducted using a single cell line, KGN. Unfortunately, this limitation is unavoidable as the KGN cell line is the only available AGCT cell line. To mitigate this limitation, we utilized multiple clones that underwent the CRISPR process, resulting in clones maintaining their original status (PARENTAL) or losing the FOXL2-C134W mutation (CRISPR).

In this study, we have demonstrated that specific disruption of the FOXL2-C134W mutation in a CRISPR-mediated manner reduces the malignant phenotype of AGCT cells and increases their susceptibility to drugs previously used for AGCT treatment. These findings strongly suggest that AGCT cells are dependent on the FOXL2-C134W mutation. Furthermore, comparison of CRISPR-edited and parental KGN cells has provided valuable insights into the underlying mechanisms involved in AGCT development and progression and propose new therapeutic strategies for their treatment.

Acknowledgements

We want to acknowledge the very important role of patients on the rare disease, scientific works. Specially, we want to deeply thank the support we found on Blanca Antuña. We would like to thank also Vanessa Lafarga for her advice and technical support on the ConnectivityMap studies. We acknowledge grade students Irene Hernández and Andrea González for their enthusiastic participation in some phases of this work. This study was supported by a Beca Gethi-Ramón de las Peñas (from Grupo Español de Tumores Huerfanos e Infrecuentes) for the Investigation on orphan and infrequent tumors, by a Semilla Grant from the Asociación Española Contra el Cáncer (AECC) and by structural funding of the Instituto de Salud Carlos III.

Conflict of interest

The authors declare no conflict of interest.

Author contributions

SA-Q acquired and analyzed most of the data. PN, AR, and AM assist with several molecular experiments. AM-C and RB performed and analyzed

proteomic studies. MJB, SM, and IC carried out transcriptomic analyses. BV-M, CE, DGD, and IH collaborate in molecular assays. PC-S and LS performed and analyzed the zebrafish studies. DM assisted in all the microscopy related experiments. JG-D and IPC developed the study concept and obtained funding. AM and IPC supervised the work, interpreted the data and drafted/edited the manuscript. All authors have read and agreed to the published version of the manuscript.

Peer review

The peer review history for this article is available at <https://www.webofscience.com/api/gateway/wos/peer-review/10.1002/1878-0261.13799>.

Data accessibility

The data supporting the findings of this study are available within the article and its Supplementary Material. The proteomics raw data have been deposited at PRIDE repository with the identifier PXD030751. Transcriptomic raw data has been deposited at GEO with the accession [GSE271552](https://www.ncbi.nlm.nih.gov/geo/query/acc.cgi?acc=GSE271552).

References

- Boyd N, Dancey JE, Gilks CB, Huntsman DG. Rare cancers: a sea of opportunity. *Lancet Oncol.* 2016;**17**(2):e52–61.
- Khosla D, Dimri K, Pandey AK, Mahajan R, Trehan R. Ovarian granulosa cell tumor: clinical features, treatment, outcome, and prognostic factors. *N Am J Med Sci.* 2014;**6**(3):133.
- McConechy MK, Färkkilä A, Horlings HM, Talhouk A, Unkila-Kallio L, van Meurs HS, et al. Molecularly defined adult granulosa cell tumor of the ovary: The clinical phenotype. *J Natl Cancer Inst.* 2016;**108**:djw134.
- Kaspar HG, Crum CP. The utility of immunohistochemistry in the differential diagnosis of gynecologic disorders. *Arch Pathol Lab Med.* 2015;**139**(1):39–54.
- Mills AM, Chinn Z, Rauh LA, Dusenbery AC, Whitehair RM, Saks E, et al. Emerging biomarkers in ovarian granulosa cell tumors. *Int J Gynecol Cancer.* 2019;**29**(3):560–5.
- Colombo N, Parma G, Zanagnolo V, Insinga A. Management of ovarian stromal cell tumors. *J Clin Oncol.* 2007;**25**(20):2944–51.
- Park JY, Jin KL, Kim DY, Kim JH, Kim YM, Kim KR, et al. Surgical staging and adjuvant chemotherapy in the management of patients with adult granulosa cell tumors of the ovary. *Gynecol Oncol.* 2012;**125**(1):80–6.
- Costa MJ, Walls J, Ames P, Roth LM. Transformation in recurrent ovarian granulosa cell tumors: ki67 (mib-1) and p53 immunohistochemistry demonstrates a possible molecular basis for the poor histopathologic prediction of clinical behavior. *Hum Pathol.* 1996;**27**:281.
- van Meurs HS, Buist MR, Westermann AM, Sonke GS, Kenter GG, van der Velden J. Effectiveness of chemotherapy in measurable granulosa cell tumors: a retrospective study and review of literature. *Int J Gynecol Cancer.* 2014;**24**(3):496–505.
- Raspagliesi F, Martinelli F, Grijuela B, Guadalupi V. Third-line chemotherapy with tyrosine kinase inhibitor (imatinib mesylate) in recurrent ovarian granulosa cell tumor: case report. *J Obstet Gynaecol Res.* 2011;**37**(12):1864–7.
- van Meurs HS, van Lonkhuijzen LRCW, Limpens J, van der Velden J, Buist MR. Hormone therapy in ovarian granulosa cell tumors: a systematic review. *Gynecol Oncol.* 2014;**134**(1):196–205.
- Garcia-Donas J, Hurtado A, Garcia-Casado Z, Albareda J, Lopez-Guerrero JA, Alemany I, et al. Cytochrome P17 inhibition with ketoconazole As treatment for advanced granulosa cell ovarian tumor. *J Clin Oncol.* 2013;**31**(10):e165–6.
- Shah SP, Köbel M, Senz J, Morin RD, Clarke BA, Wiegand KC, et al. Mutation of *FOXL2* in granulosa-cell tumors of the ovary. *N Engl J Med.* 2009;**360**(26):2719–29.
- Jamieson S, Butzow R, Andersson N, Alexiadis M, Unkila-Kallio L, Heikinheimo M, et al. The *FOXL2* C134W mutation is characteristic of adult granulosa cell tumors of the ovary. *Mod Pathol.* 2010;**23**(11):1477–85.
- Beysen D, De Paepe A, De Baere E. *FOXL2* mutations and genomic rearrangements in BPES. *Hum Mutat.* 2009;**30**(2):158–69.
- Udar N, Yellore V, Chalukya M, Yelchits S, Silva-Garcia R, Small K, et al. Comparative analysis of the *FOXL2* gene and characterization of mutations in BPES patients. *Hum Mutat.* 2003;**22**(3):222–8.
- De Baere E, Dixon MJ, Small KW, Jabs EW, Leroy BP, Devriendt K, et al. Spectrum of *FOXL2* gene mutations in blepharophimosis-ptosis-epicanthus inversus (BPES) families demonstrates a genotype-phenotype correlation. *Hum Mol Genet.* 2001;**10**(15):1591–600.
- Benayoun BA, Dipietromaria A, Bazin C, Veitia RA. *FOXL2*: at the crossroads of female sex determination and ovarian function. *Adv Exp Med Biol.* 2009;**665**:207–26.
- Uda M, Ottolenghi C, Crisponi L, Garcia JE, Deiana M, Kimber W, et al. *Foxl2* disruption causes mouse ovarian failure by pervasive blockage of follicle development. *Hum Mol Genet.* 2004;**13**(11):1171–81.
- Cocquet J, Pailhous E, Jaubert F, Servel N, Xia X, Pannetier M, et al. Evolution and expression of *FOXL2*. *J Med Genet.* 2002;**39**(12):916–21.

- 21 Uhlenhaut NH, Jakob S, Anlag K, Eisenberger T, Sekido R, Kress J, et al. Somatic sex reprogramming of adult ovaries to testes by FOXL2 ablation. *Cell*. 2009;**139**(6):1130–42.
- 22 Baddela VS, Michaelis M, Tao X, Koczan D, Vanselow J. ERK1/2-SOX9/FOXL2 axis regulates ovarian steroidogenesis and favors the follicular–luteal transition. *Life Sci Alliance*. 2023;**6**(10):e202302100.
- 23 Odle AK, Childs GV. SMAD-FOXL2 regulation of FSHB: a game of human and mouse. *Endocrinology*. 2020;**161**(7):bqaa077.
- 24 Li J, Bao R, Peng S, Zhang C. The molecular mechanism of ovarian granulosa cell tumors. *J Ovarian Res*. 2018;**11**(1):13.
- 25 Batista F, Vaiman D, Dausset J, Fellous M, Veitia RA. Potential targets of FOXL2, a transcription factor involved in craniofacial and follicular development, identified by transcriptomics. *Proc Natl Acad Sci USA*. 2007;**104**(9):3330–5.
- 26 Weis-Banke SE, Lerdrup M, Kleine-Kohlbrecher D, Mohammad F, Sidoli S, Jensen ON, et al. Mutant FOXL2C134W hijacks SMAD4 and SMAD2/3 to drive adult granulosa cell tumors. *Cancer Res*. 2020;**80**(17):3466–79.
- 27 Nishi Y, Yanase T, Mu YM, Oba K, Ichino I, Saito M, et al. Establishment and characterization of a steroidogenic human granulosa-like tumor cell line, KGN, that expresses functional follicle-stimulating hormone receptor. *Endocrinology*. 2001;**142**(1):437–45.
- 28 Martín A, Epifano C, Vilaplana-Martí B, Hernández I, Macías RIR, Martínez-Ramírez Á, et al. Mitochondrial RNA methyltransferase TRMT61B is a new, potential biomarker and therapeutic target for highly aneuploid cancers. *Cell Death Differ*. 2022;**30**(1):37–53.
- 29 Montero-Calle A, Garranzo-Asensio M, Rejas-González R, Feliu J, Mendiola M, Peláez-García A, et al. Benefits of FAIMS to improve the proteome coverage of deteriorated and/or cross-linked TMT 10-Plex FFPE tissue and plasma-derived exosomes samples. *Proteomes*. 2023;**11**(4):35.
- 30 Montero-Calle A, Jiménez de Ocaña S, Benavente-Naranjo R, Rejas-González R, Bartolomé RA, Martínez-Useros J, et al. Functional proteomics characterization of the role of SPRYD7 in colorectal cancer progression and metastasis. *Cells*. 2023;**12**(21):2548.
- 31 Solís-Fernández G, Montero-Calle A, Martínez-Useros J, López-Janeiro Á, de los Ríos V, Sanz R, et al. Spatial proteomic analysis of isogenic metastatic colorectal cancer cells reveals key dysregulated proteins associated with lymph node, liver, and lung metastasis. *Cells*. 2022;**11**(3):447.
- 32 Montero-Calle A, López-Janeiro Á, Mendes ML, Perez-Hernandez D, Echevarría I, Ruz-Caracuel I, et al. In-depth quantitative proteomics analysis revealed CIGALT1 depletion in ECC-1 cells mimics an aggressive endometrial cancer phenotype observed in cancer patients with low CIGALT1 expression. *Cell Oncol*. 2023;**46**(3):697–715.
- 33 Subramanian A, Tamayo P, Mootha VK, Mukherjee S, Ebert BL, Gillette MA, et al. Gene set enrichment analysis: a knowledge-based approach for interpreting genome-wide expression profiles. *Proc Natl Acad Sci U S A*. 2005;**102**(43):15545–50.
- 34 Shin E, Jin H, Suh D, Luo Y, Ha H, Kim TH, et al. An alternative miRISC targets a cancer-associated coding sequence mutation in FOXL2. *EMBO J*. 2020;**39**(24):e104719.
- 35 Haltia UM, Andersson N, Yadav B, Färkkilä A, Kuleskiy E, Kankainen M, et al. Systematic drug sensitivity testing reveals synergistic growth inhibition by dasatinib or mTOR inhibitors with paclitaxel in ovarian granulosa cell tumor cells. *Gynecol Oncol*. 2017;**144**(3):621–30.
- 36 Garcia-Donas J, Hurtado A, Garrigos L, Santaballa A, Redondo A, Vidal L, et al. Open-label phase II clinical trial of ketoconazole as CYP17 inhibitor in metastatic or advanced non-resectable granulosa cell ovarian tumors: the GREKO (GRanulosa et KetOconazole) trial, GETHI 2011-03. *Clin Transl Oncol*. 2023;**25**(7):2090–8.
- 37 Westerfield M. The Zebrafish Book. A guide for the laboratory use of zebrafish (*Danio rerio*). 5th ed. Eugene, OR, USA: Univ Oregon Press; 2007.
- 38 Stirling DR, Suleyman O, Gil E, Elks PM, Torraca V, Noursadeghi M, et al. Analysis tools to quantify dissemination of pathology in zebrafish larvae. *Sci Rep*. 2020;**10**(1):3149.
- 39 Frost ER, Taylor G, Boeing S, Galichet C, Baker MA, Sutherland JM, et al. p27 kip1-dependent gene activity within granulosa cells reveals pathways relevant for control of primordial follicle activation in mice. *bioRxiv*. <https://doi.org/10.1101/2022.10.24.513438>
- 40 Gustin SE, Hogg K, Stringer JM, Rastetter RH, Pelosi E, Miles DC, et al. WNT/ β -catenin and p27/FOXL2 differentially regulate supporting cell proliferation in the developing ovary. *Dev Biol*. 2016;**412**(2):250–60.
- 41 Prasad SB, Yadav SS, Das M, Modi A, Kumari S, Pandey LK, et al. PI3K/AKT pathway-mediated regulation of p27Kip1 is associated with cell cycle arrest and apoptosis in cervical cancer. *Cell Oncol*. 2015;**38**(3):215–25.
- 42 Färkkilä A, Haltia U-M, Tapper J, McConechy MK, Huntsman DG, Heikinheimo M. Pathogenesis and treatment of adult-type granulosa cell tumor of the ovary. *Ann Med*. 2017;**49**(5):435–47.
- 43 Bryk S, Färkkilä A, Bützow R, Leminen A, Tapper J, Heikinheimo M, et al. Characteristics and outcome of recurrence in molecularly defined adult-type ovarian

- granulosa cell tumors. *Gynecol Oncol.* 2016;**143**(3):571–7.
- 44 Chen X, Li Y, Yao T, Jia R. Benefits of zebrafish xenograft models in cancer research. *Front Cell Dev Biol.* 2021;**9**:9.
- 45 Park M, Shin E, Won M, Kim J-H, Go H, Kim H-L, et al. FOXL2 interacts with steroidogenic Factor-1 (SF-1) and represses SF-1-induced *CYP17* transcription in granulosa cells. *Mol Endocrinol.* 2010;**24**(5):1024–36.
- 46 Rosario R, Araki H, Print CG, Shelling AN. The transcriptional targets of mutant FOXL2 in granulosa cell Tumours. *PLoS One.* 2012;**7**(9):e46270.
- 47 Llano E, Todeschini AL, Felipe-Medina N, Corte-Torres MD, Condezo YB, Sanchez-Martin M, et al. The oncogenic FOXL2 C134W mutation is a key driver of granulosa cell tumors. *Cancer Res.* 2023;**83**(2):239–50.
- 48 Ni N, Fang X, Mullens DA, Cai JJ, Ivanov I, Bartholin L, et al. Transcriptomic profiling of gene expression associated with granulosa cell tumor development in a mouse model. *Cancers.* 2022;**14**(9):2184.
- 49 Abedel-Majed MA, Romereim SM, Davis JS, Cupp AS. Perturbations in lineage specification of granulosa and theca cells may Alter corpus luteum formation and function. *Front Endocrinol.* 2019;**10**:832.
- 50 Wen F, Ding Y, Wang M, Du J, Zhang S, Kee K. FOXL2 and NR5A1 induce human fibroblasts into steroidogenic ovarian granulosa-like cells. *Cell Prolif.* 2024;**57**:e13589. <https://doi.org/10.1111/cpr.13589>
- 51 Kuo FT, Fan K, Bentsi-Barnes I, Barlow GM, Pisarska MD. Mouse forkhead L2 maintains repression of FSH-dependent genes in the granulosa cell. *Reproduction.* 2012;**144**(4):485–94.
- 52 Strushkevich N, MacKenzie F, Cherkesova T, Grabovec I, Usanov S, Park HW. Structural basis for pregnenolone biosynthesis by the mitochondrial monooxygenase system. *Proc Natl Acad Sci USA.* 2011;**108**(25):10139–43.
- 53 Georges A, L'Hôte D, Todeschini AL, Auguste A, Legois B, Zider A, et al. The transcription factor FOXL2 mobilizes estrogen signaling to maintain the identity of ovarian granulosa cells. *eLife.* 2014;**3**:3.
- 54 Kim S-Y, Weiss J, Tong M, Laronda MM, Lee E-J, Jameson JL. Foxl2, a Forkhead transcription factor, modulates nonclassical activity of the estrogen receptor- α . *Endocrinology.* 2009;**150**(11):5085–93.
- 55 Moumné L, Batista F, Benayoun BA, Nallathambi J, Fellous M, Sundaresan P, et al. The mutations and potential targets of the forkhead transcription factor FOXL2. *Mol Cell Endocrinol.* 2008;**282**:2–11.
- 56 Subramanian A, Narayan R, Corsello SM, Peck DD, Natoli TE, Lu X, et al. A next generation connectivity map: L1000 platform and the first 1,000,000 profiles. *Cell.* 2017;**171**(6):1437–52.
- 57 Da Cruz PA, da Silva EM, Segura SE, Pareja F, Bi R, Selenica P, et al. Genomic profiling of primary and recurrent adult granulosa cell tumors of the ovary. *Mod Pathol.* 2020;**33**(8):1606–17.
- 58 Tang B, Zhang Y, Zhang W, Zhu Y, Yuan S. Deletion of FOXL2 by CRISPR promotes cell cycle G0/G1 restriction in KGN cells. *Int J Mol Med.* 2019;**43**(1):567–74.
- 59 Herman L, Amo A, Legois B, Di Carlo C, Veitia RA, Todeschini AL. A cellular model provides insights into the pathogenicity of the oncogenic FOXL2 somatic variant p.Cys134Trp. *Br J Cancer.* 2024;**130**:1453–62. <https://doi.org/10.1038/s41416-024-02613-x>
- 60 Bursac S, Prodan Y, Pullen N, Bartek J, Volarevic S. Dysregulated ribosome biogenesis reveals therapeutic liabilities in cancer. *Trends Cancer.* 2021;**7**(1):57–76.

Supporting information

Additional supporting information may be found online in the Supporting Information section at the end of the article.

Fig. S1. Edition of FOXL2 c.402C>G mutation in KGN cells upon transfection of CRISPR/Cas9 complexes. (A) Timeline for the generation of pools (P) and clones (C) after the electroporation of CRISPR/Cas9 complexes. (B) Analysis of the specificity of the guide RNAs for the FOXL2 c.402C>G mutant allele. Graph represents percentage of reads matching each edited and not edited alleles for the pool of nucleofected cells for each condition. The bottom table shows the numerical data of the graph. (C) Indels identified in nucleofected pools, upon activity of each CRISPR/Cas9 complex.

Fig. S2. Characterization of null clones and CRISPR-edited clones in which only wild type allele can be detected. Panels A–D present data in Figure 2(A–D), separating CRISPR-edited clones and clones with only the WT allele, and including results from the two FOXL2-null clones isolated in this study. Panels E and F similarly separate clone types to display data from Figures 4A and 5A, respectively. In most assays, KO null cells and WT-only clones behave similarly to CRISPR clones; however, principal component analysis (PCA) of transcriptomic data reveals a distinct expression signature for the two KO clones compared to both CRISPR-edited and parental lines.

Fig. S3. Overexpression of FOXL2-WT and FOXL2-mutant alleles in KGN cells depleted from C134W mutation. Using primer pairs as described by Shin et al. [34], we selectively amplified and quantified FOXL2-WT and FOXL2-MUT alleles in both

PARENTAL (blue, $n = 4$) and CRISPR (orange, $n = 5$) clones. Average expression values are shown. The right panel provides details on the status of the MUT allele in the CRISPR clones used, along with specific reverse primer locations and edited nucleotide positions. A significant overexpression of the WT allele is observed in CRISPR clones compared to PARENTAL cells. Even greater overexpression is detected for the MUT allele in CRISPR clones where the MUT allele remains amplifiable (#15 and #20).

Fig. S4. Flow cytometry cell cycle analysis of PARENTAL and CRISPR clones. Cell cycling profiling was determined by PI-staining and flow cytometry analysis. Data were analyzed with Floreada.io (<https://floreada.io/analysis>). Graphs show cell cycle profiles of PARENTAL ($n = 5$) and CRISPR ($n = 11$) clones.

Fig. S5. Validation by RT-qPCR of transcriptomic data. Graphs show the results from quantitative PCR results of genes included in the transcriptomic study. Transcriptomic information from the RNAseq experiment (Figure 5) is included in the bottom right table.

Fig. S6. Clustering analyses of transcriptomic data from tumoral and non-tumoral granulosa cell clones. PARENTAL [KGN(GT)] and CRISPR [CRISPR(GT)] clones from this study are compared with KGN and HGrC1 granulosa cell lines generated by Weis-Banke et al [26]: [KGN (W-B)], [HGrC1 (ev)], [HGrC1 (FOXL2-mut)] and [HGrC1 (FOXL2-wt)]. KGN/PARENTAL genotype cells are marked in blue, and CRISPR/Edited/WT cells are colored in orange.

Fig. S7. Network clustering of proteomic GO terms from differential expressed proteins. Up and down-regulated, GO terms at q -value < 0.05 are shown.

Fig. S8. Comparison of the effects induced by Palbociclib and BRD6929 in PARENTAL and CRISPR clones. Quantification of cell death (A) and cell number (B) is shown for both PARENTAL ($n = 5$) and CRISPR ($n = 6$) clones, 24 h after treatment with palbociclib or BRD6929. Values are normalized to those of untreated cells. Near-significant comparisons are indicated with exact P values.

Table S1. Genomic analysis from pools after gene edition.

Table S2. Indels characterization of the reads obtained from amplicon Deep sequencing of the pools after gene edition.

Table S3. List of clones generated from pools edited with guides sg1.3 and sg1.4.

Table S4. List of the DEG found in PARENTAL, KGN clones when compared with CRISPR ones.

Table S5. List of top25 up (red) and top25 down (blue) regulated genes differentially expressed between PARENTAL and CRISPR clones.

Table S6. List of the DEPs found in KGN clones when compared with CRISPR ones.

Table S7. Genes commonly de-regulated in the transcriptomic and proteomic analyses.

Table S8. List of top25 up (red) and down (blue) regulated proteins differentially expressed between PARENTAL and CRISPR clones.

Table S9. cMap first 100 ranked compounds that mimic the expression signature induced in KGN cells upon the elimination of FOXL2-C134W mutation.

Table S10. Types of compounds that mimic the expression signature induced in KGN cells upon the elimination of FOXL2-C134W mutation.